Electronic Supporting Information (ESI)

TABLE OF CONTENTS

Experimental section

Materials

All chemicals were of reagent grade quality. They were purchased from commercial sources and used as received. Compounds **6**–**9** were prepared as reported in the preceding paper.[1]

Preparation of ligands and complexes

4-MePhPDI. A mixture of pyridine-2,6-diformaldehyde (0.135 g, 1.0 mmol) and aniline (181 µL, 2.0 mmol) in 5.0 mL of ethanol under the presence of 100 µL of acetic acid was allowed to reflux for 30 min. The mixture was cooled in an ice bath leading to a white crystalline powder, which was filtered and washed with a small quantity of ethanol. Yield 84%. Anal. Calc. for $C_{21}H_{19}N_3$ (4-MePhPDI): C, 80.48; H, 6.11; N, 13.41. Found: C, 80.96; H, 5.87; N, 13.75%. IR (KBr, cm^{-1}): 2916(m) [ν(C–H) from methyl substituent of 4-MePhPDI ligand], 1624(m) [ν(C=N) from 4-MePhPDI ligand]. ^{1}H NMR ($CDCl_3$; 300 MHz, ppm): δ = 8.70 (s, 2H, H_{im}), 8.27 (d, 2H, *p*-H_{py}, J = 7.8 Hz), 7.92 (t, 1H, *m*-H_{py}, J = 7.8 Hz), 7.27 (d, 4H, *o*-H_{Ph}, J = 8.9 Hz), 7.23 (d, 4H, *m*-H_{Ph}, J = 8.9 Hz), 2.39 (s, 6H, *p*-H_{Me}).

4-MeOPhPDI. A mixture of pyridine-2,6-diformaldehyde (0.135 g, 1.0 mmol) and *p*-anisidine (0.246 g, 2.0 mmol) in 5.0 mL of ethanol under the presence of 100 µL of acetic acid was allowed to reflux for 30 min. The mixture was cooled in an ice bath leading to a brownish crystalline powder, which was filtered and washed with a small quantity of ethanol. Yield 88%. Anal. Calc. for $C_{21}H_{19}N_3O_2$ (4-MeOPhPDI): C, 73.03; H, 5.54; N, 12.17. Found: C, 73.94; H, 5.13; N, 12.29%. IR (KBr, cm^{-1}): 2965(w) [ν(C–H) from methoxy substituent of 4-MeOPhPDI ligand], 1624(m) [ν(C=N) from 4-MeOPhPDI ligand], 1245(s) [ν(C–O) from methoxy substituent of 4-MeOPhPDI ligand]. ^{1}H NMR ($CDCl_3$; 300 MHz, ppm): δ = 8.70 (s, 2H, H_{im}), 8.24 (d, 2H, *p*-H_{py}, J = 7.8 Hz), 7.90 (t, 1H, *m*-H_{py}, J = 7.8 Hz), 7.36 (d, 4H, *o*-H_{Ph}, J = 8.9 Hz), 6.96 (d, 4H, *m*-H_{Ph}, J = 8.9 Hz), 3.85 (s, 6H, *p*-H_{OMe}).

4-MeSPhPDI. A mixture of pyridine-2,6-diformaldehyde (0.135 g, 1.0 mmol) and 4-(methylthio)aniline (250 µL, 2.0 mmol) in 5.0 mL of ethanol under the presence of 100 µL of acetic acid was allowed to reflux for 30 min. The mixture was cooled in an ice bath leading to a yellowish crystalline powder, which was filtered and washed with a small quantity of ethanol. Yield 88%. Anal. Calc. for $C_{21}H_{19}N_3S_2$ (4-MeSPhPDI): C, 66.81; H, 5.07; N, 11.13. Found: C, 66.95; H, 5.04; N, 11.42%. IR (KBr, cm^{-1}): 2916(m) [ν(C–H) from thiomethyl substituent of 4-MeSPhPDI ligand], 1621(m) [ν(C=N) from 4-MeSPhPDI ligand]. ^{1}H NMR ($CDCl_3$; 300 MHz, ppm): δ = 8.67 (s, 2H, H_{im}), 8.24 (d, 2H, *p*-H_{py}, J = 7.8 Hz), 7.90 (t, 1H, *m*-H_{py}, J = 7.8 Hz), 7.23 (d, 4H, *o*-H_{Ph}, J = 8.9 Hz), 6.94 (d, 4H, *m*-H_{Ph}, J = 8.9 Hz), 2.47 (s, 6H, *p*-H_{SMe}).

4-Me$_2$NPhPDI. A mixture of pyridine-2,6-diformaldehyde (0.135 g, 1.0 mmol) and *N*,*N*-dimethyl-*p*-phenylenediamine (0.272 g, 2.0 mmol) in 5.0 mL of ethanol under the presence of 100 µL of acetic acid was allowed to reflux for 30 min. The mixture was cooled in an ice bath leading to a green powder, which was filtered and washed with a small quantity of ethanol. Yield 77%. Anal. Calc. for $C_{23}H_{25}N_5$ (4-Me$_2$NPhPDI): C, 74.36; H, 6.78; N, 18.85%. Found: C, 73.84; H, 6.95; N, 18.90%. IR (KBr, cm^{-1}): 2882(s) [ν(C–H) from dimethylamine substituent of 4-Me$_2$NPhPDI ligand], 1618(m) [ν(C=N) from 4-Me$_2$NPhPDI ligand]. ^{1}H NMR ($CDCl_3$; 300 MHz, ppm): δ = 8.74 (s, 2H, H_{im}), 8.21 (d, 2H, *p*-H_{py}, J = 7.8 Hz), 7.86 (t, 1H, *m*-H_{py}, J = 7.8 Hz), 7.40 (d, 4H, *o*-H_{Ph}, J = 8.9 Hz), 6.77 (d, 4H, *m*-H_{Ph}, J = 8.9 Hz), 3.01 (s, 12H, *p*-H_{NMe2}).

[1] R. Rabelo, L. Toma, M. Julve, F. Lloret, J. Pasán, D. Cangussu, R. Ruiz-García and Joan Cano, *Dalton Trans*., 2024, **53**, 5507.

2,4-Me$_2$PhPDI. A mixture of pyridine-2,6-diformaldehyde (0.135 g, 1.0 mmol) and 2,4-dimethylaniline (247 μL, 2.0 mmol) in 5.0 mL of ethanol under the presence of 100 μL of acetic acid was allowed to reflux for 30 min. The mixture was cooled in an ice bath leading to a yellow crystalline powder, which was filtered and washed with a small quantity of ethanol. Yield 85%. Anal. Calc. for $C_{23}H_{23}N_3$ (2,4-Me$_2$PhPDI): C, 80.90; H, 6.79; N, 12.31. Found: C, 80.72; H, 6.62; N 12.65%. IR (KBr, cm^{-1}): 2914(s) [ν(C–H) from methyl substituent of 2,4-Me$_2$PhPDI ligand], 1626(m) [ν(C=N) from 2,4-Me$_2$PhPDI ligand]. ^{1}H NMR ($CDCl_3$; 300 MHz, ppm): δ = 8.60 (s, 2H, H_{im}), 8.32 (d, 2H, *p*-H_{py}, J = 7.8 Hz), 7.92 (t, 1H, *m*-H_{py}, J = 7.8 Hz), 7.04 (m, 3H, *o*- and *m*-H_{Ph}), 2.40 (s, 3H, *o*-H_{Me}), 2.35 (s, 3H, *p*-H_{Me}).

*[Co(4-MePhPDI)$_2$](ClO$_4$)$_2$·H$_2$O (**1**).* 4-MePhPDI (0.032 g, 0.10 mmol) was suspended in ethanol (10 mL). To this mixture was slowly added an ethanolic solution (2.0 mL) of cobalt(II) perchlorate hexahydrate (0.018 g, 0.05 mmol). The resulting red solution was evaporated at room temperature and red needles of **1** appeared on the very next day. They were collected and dried over filter paper. Yield 65%. Anal. Calc. for $C_{42}H_{40}N_6O_9Cl_2Co$ (**1**): C, 54.43; H, 3.98; N, 9.77. Found: C, 53.92; H, 4.02; N, 9.65%. IR (KBr, cm^{-1}): 3426(s) [ν(O–H) from crystallization water], 2920(m) [ν(C–H) from methyl substituent of 4-MePhPDI ligand], 1596(m) [ν(C=N) from 4-MePhPDI ligand], 1088(vs) [ν(Cl–O) from perchlorate anion]. UV-Vis (MeCN): ν_{max} = 51282 cm^{-1} (ε = 108743 M^{-1}cm^{-1}), 44445 (56561), and 28490 (29118).

*[Co(4-MeOPhPDI)$_2$](ClO$_4$)$_2$ (**2**).* 4-MeOPhPDI (0.017 g, 0.05 mmol) was dissolved in chloroform (0.5 mL) and putted in the bottom of a glass tube. A 4:1 mixture of methanol/chloroform (8.0 mL) was slowly added to allow for a separation of the solutions. A methanolic solution (0.5 mL) of cobalt(II) perchlorate hexahydrate (0.010 g, 0.025 mmol) was added on the top of the tube. X-ray suitable red plates of **2** were grown through slow diffusion after a few days. Yield 82%. Anal. Calc. for $C_{41}H_{35}N_6O_{12}Cl_2Co$ (**2**): C, 53.18; H, 4.04; N, 8.86. Found: C, 53.98; H, 4.17; N, 8.90%. IR (KBr, cm^{-1}): 2973(m) [ν(C–H) from methoxy substituent of 4-MeOPDI ligand], 1596(s) [ν(C=N) from 4-MeOPDI ligand], 1082(vs) [ν(Cl–O) from perchlorate anion]. UV-Vis (MeCN): ν_{max} = 51282 cm^{-1} (ε = 99048 M^{-1}cm^{-1}), 44248 (59889), and 26385 (28780).

*[Co(4-MeSPhPDI)$_2$](ClO$_4$)$_2$ (**3**).* An ethanol solution (2.0 mL) of cobalt(II) perchlorate hexahydrate (0.035 g, 0.10 mmol) was added dropwise to a suspension of 4-MeSPhPDI (0.075 g, 0.20 mmol) in ethanol (20.0 mL) under stirring. The mixture was further stirred for one hour under gentle warming. The resulting polycrystalline powder was filtered and washed with a small quantity of ethanol. X-ray quality dark red crystals of **3** were obtained by slow diffusion of ethyl acetate on a saturated chloroform/acetonitrile solution (1:1) of the polycrystalline powder in a glass tube. Yield 90%. Anal. Calc. for $C_{41}H_{35}N_6O_{12}Cl_2Co$ (**3**): C, 49.80; H, 3.78; N, 8.30. Found: C, 50.12; H, 3.84; N, 8.45%. IR (KBr, cm^{-1}): 2919(w) [ν(C–H) from the thiomethyl substituents of 4-MeSPhPDI], 1585(s) [ν(C=N) from the imine groups of 4-MeSPhPDI], 1093(vs) [ν(Cl–O) from perchlorate anion].

*[Co(4-Me$_2$NPhPDI)$_2$](ClO$_4$)$_2$·1/2H$_2$O (**4**).* Cobalt(II) perchlorate hexahydrate (0.037 g, 0.1 mmol) was dissolved in methanol (5.0 mL) and added dropwise to a 4-Me$_2$NPhPDI (0.0635 g, 0.2 mmol) suspension in methanol (20.0 mL). The dark purple solution was allowed to evaporate at room temperature and black block-like crystals of **4** appeared after one week. They were collected and dried over filter paper. Yield 76%. Anal. Calc. for $C_{46}H_{51}N_{10}O_{8.5}Cl_2Co$ (**4**): C, 54.71; H, 5.09; N, 13.87; Found: C, 54.72; H, 4.97; N, 14.05%. IR (KBr, cm^{-1}): 3434(w) [ν(O–H) from crystallization water], 2892(w) [ν(C–H) from dimethylamine substituent of 4-Me$_2$NPhPDI ligand], 1608(s) [ν(C=N) from 4-Me$_2$NPDI ligand], 1094(vs) [ν(Cl–O) from perchlorate anion]. UV-Vis (MeCN): ν_{max} = 50252 cm^{-1} (ε = 95194 M^{-1}cm^{-1}), 38760 (49366), and 20450 (38164).

*[Co(2,4-Me$_2$PhPDI)$_2$](ClO$_4$)$_2$ (**5**).* Cobalt(II) perchlorate hexahydrate (0.037 g, 0.1 mmol) was dissolved in methanol (5.0 mL) and added dropwise to a 2,4-Me$_2$PhPDI (0.0684 g, 0.2 mmol) suspension in methanol (10.0 mL). The red solution was allowed to evaporate at room temperature and red needles of **5** appeared at the very next day. They were collected and dried over filter paper. Yield 72%. Anal. Calc. for $C_{45}H_{42}N_6O_8Cl_2Co$ (**5**): C, 58.73; H, 4.93; N, 8.93; Found: C, 58.92; H,

4.74; N, 9.45%. IR (KBr, cm^{-1}): 2921(s) [ν(C–H) from methyl substituent of 2,4-Me_2PhPDI ligand], 1600(s) [ν(C=N) from 2,4-Me_2PhPDI ligand], 1091(vs) [ν(Cl–O) from perchlorate anion]. UV-Vis (MeCN): ν_{max} = 51021 cm^{-1} (ε = 115934 $M^{-1}cm^{-1}$), 42554 (48508), and 29240 (20132).

Physical techniques

Elemental analyses (C, H, N) were performed at the Servicio Central de Soporte a la Investigación (SCSIE) at the Universitat de València (Spain). FT–IR spectra were recorded on a Nicolet-5700 spectrophotometer as solid KBr pellets. Electronic absorption spectra of the ligands and complexes **1**–**5** were recorded in acetonitrile solutions (5.0×10^{-3} mM) at room temperature with a Jasco UV/Vis/NIR V-670 spectrophotometer. ^{1}H NMR spectra were recorded at room temperature on a Bruker AC 300 (300 MHz) spectrometer. Deuterated chloroform was used as solvent and internal standard (δ = 7.26 ppm). X- and Q-band EPR spectra (ν = 9.4 and 34.03 GHz) of crushed crystal samples of **1**–**5** were recorded at 4.0 K under non-saturating conditions with a Bruker ER 200 D spectrometer equipped with a helium-flow cryostat. Powder X-ray diffraction (XRD) patterns of crushed crystal samples were collected at room temperature on a D8 Avance A25 Bruker diffractometer using graphite-monochromated Cu-Kα radiation (λ = 1.54056 Å).

Electrochemical measurements

Cyclic voltammetry studies were performed using an AUTOLAB 204 scanning potentiostat operating at a scan rate of 20–250 mV s^{-1}. Cyclic voltammograms were collected at room temperature using 0.1 M nBu$_4$NPF$_6$ as supporting electrolyte and 1.0 mM of **1**–**9** in acetonitrile. The working electrode was a platinum disk (0.32 cm^2), while the reference electrode was AgCl/Ag, and a glassy carbon rod (76 mm) was used as auxiliary electrode. All experiments were performed in standard electrochemical cells under argon. The investigated potential range was in the range of –2.0 to +2.0 V *vs* AgCl/Ag. Ferrocene was added as internal standard at the end of the measurements. The formal potentials were measured at a scan rate of 200 mV s^{-1}, and they were calibrated against the ferrocenium/ferrocene (Fc^+/Fc) couple. The values of the measured formal potential and the anodic to cathodic peaks separation of ferrocene under the same conditions are E(Fc^+/Fc) = +0.40 V *vs* AgCl/Ag and $\Delta E_{p(Fc+/Fc)}$ = 80 mV (CH_3CN, 0.1 M nBu$_4$NPF$_6$, 25 °C).

Magnetic measurements

Variable-temperature (T = 2.0–300 K) direct current (dc) magnetic susceptibility measurements under applied fields of 0.25 (T < 20 K) and 5.0 kOe (T > 20 K) and variable-field (H = 0–50 kOe) magnetisation measurements in the temperature range of 2.0–10 K were carried out on crushed crystals of **1**–**5** with a Quantum Design SQUID magnetometer. The magnetic susceptibility data were corrected for the diamagnetism of the constituent atoms and the sample holder. Variable-temperature (T = 2.0–10 K) alternating current (ac) magnetic susceptibility measurements under ±5.0 Oe oscillating field at frequencies in the range of 0.1–10 kHz were performed under different applied static dc fields (H_{dc} = 0–2.5 kOe) with a Quantum Design Physical Property Measurement System (PPMS).

Crystal structure data collection and refinement

X-ray diffraction data of single crystals of **1** and **2** were collected on an Agilent Supernova diffractometer equipped with an EosS2 detector with Mo-Kα radiation (λ = 0.71073 Å) at 100 (**1**) and 150 K (**2**). The data for **3**–**4** were collected on a Bruker D8 Venture diffractometer with a PHOTON II detector by using monochromatic Mo-Kα radiation (λ = 0.71073 Å) at 150 K, whereas that of **5** was collected on an Agilent Supernova diffractometer equipped with an Atlas detector with Cu-Kα radiation (λ = 1.54184 Å) at 100 K. Diffraction data of **1**–**5** were collected, scaled, and integrated

using the CrysAlisPro software[2] for **1**, **2**, and **5**, and Bruker SAINT[3] for **3** and **4**. The structures were solved by intrinsic phasing methods integrated into the SHELXTL software[4] with the Olex2 platform.[5] The obtained models were refined with version 2018/3 of SHELXL against F^2 on all data by full-matrix least squares. All non-hydrogen atoms were anisotropically refined. The hydrogen atoms were set in geometrical position and refined with a riding model, except those of the crystallization water molecules, which were neither found nor set. Compounds **3** and **4** exhibited partial disorder in some fragments, specifically, one perchlorate anion in **3**, two perchlorate anions, and one dimethylaminophenyl group in **4**, all occupying two positions. Constraints were applied to the anisotropic displacements of the carbon atoms to model the organic fragment in these positions. The site occupancy factors (s.o.f.) refined for N9 and N9A were 0.239(5) and 0.761(5). In the case of perchlorate anions, restraints were applied to the Cl–O bond lengths and the anisotropic displacements of the oxygen and chlorine atoms to facilitate the convergence of the refinement process. The graphical manipulations and calculations were performed with the Crystalmaker[6] and Mercury[7] programs. Crystal structure figures in the manuscript and ESI were generated with CrystalMaker.[6]

Crystallographic data (excluding structure factors) of **1**–**5** have been deposited with the Cambridge Crystallographic Data Centre as supplementary publication number CCDC–2333341 (**1**), –1989325 (**2**), –2333343 (**3**), –2333342 (**4**), and –2333340 (**5**). Copies of the data can be obtained free of charge from The *Cambridge Crystallographic Data* Centre via www.ccdc.cam.ac.uk/structures.

[2] Agilent. *CrysAlis PRO*. Agilent Technologies Ltd, Yarnton, Oxfordshire, England, 2014.

[3] Bruker. *SAINT.* Bruker AXS Inc., Madison, Wisconsin, USA, 2012.

[4] G. M. Sheldrick, *Acta Cryst.,* 2015, **A71**, 3.

[5] O. V. Dolomanov, L. J. Bourhis, R. J. Gildea, J. A. K. Howard and H. J. Puschmann, *Appl. Cryst*., 2009, **42**, 339.

[6] *CrystalMaker*, CrystalMaker Software, Bicester, England, 2015.

[7] *Mercury*, The Cambridge Crystallographic Data Centre, Cambridge, UK.

Computational details

DFT study: geometries, electronic transitions and NMR chemical shifts

This study was carried out by density functional theory (DFT) calculations through the Gaussian 09 package by using the hybrid B3LYP functional,[8,9] and the quadratic convergence approach. Ahlrichs' triple-ζ with a p polarization function (TZVP) was used for all atoms in the optimized geometries of ligands and the evaluation of their electronic properties.[10,11] In the optimisation of the geometry of the cobalt(II) complex in **4**, the same basis set was used for cobalt atom but an Ahlrichs' double-ζ basis set with a polarization function (SVP) was employed for the non-metal atoms in order to reduce the cpu time. A polarizable continuum model (PCM) was used with the parameters corresponding to the acetonitrile in order to avoid the usual electronic overdelocalisation in DFT calculations.[12] Dichloromethane parameters were used in the evaluation of the NMR chemical shifts. Optimised geometries were then confirmed as global minima by frequency calculations. Electronic transitions were analysed from calculations based on the time-dependent (TD) formalism applied to the density functional theory (TDDFT).[13,14] NMR shielding tensors were computed with the gauge-independent atomic orbital (GIAO) method.[15,16,17,18] Independently, the ^{1}H NMR spectrum of tetramethylsilane (TMS) was calculated to be used as reference. The magnetic coupling states were obtained from the relative energies of several broken-symmetry (BS, RadCoRad: |–+–>, |–++>, and |++–>) functions from the high-spin state with parallel local spin moments (|+++>). More details

---

[8] M. J. Frisch, G. W. Trucks, H. B. Schlegel, G. E. Scuseria, M. A. Robb, J. R. Cheeseman, G. Scalmani, V. Barone, B. Mennucci, G. A. Petersson, H. Nakatsuji, M. Caricato, X. Li, H. P. Hratchian, A. F. Izmaylov, J. Bloino, G. Zheng, J. L. Sonnenberg, M. Hada, M. Ehara, K. Toyota, R. Fukuda, J. Hasegawa, M. Ishida, T. Nakajima, Y. Honda, O. Kitao, H. Nakai, T. Vreven, J. A. Montgomery Jr., J. E. Peralta, F. Ogliaro, M. Bearpark, J. J. Heyd, E. Brothers, K. N. Kudin, V. N. Staroverov, R. Kobayashi, J. Normand, K. Raghavachari, A. Rendell, J. C. Burant, S. S. Iyengar, J. Tomasi, M. Cossi, N. Rega, J. M. Millam, M. Klene, J. E. Knox, J. B. Cross, V. Bakken, C. Adamo, J. Jaramillo, R. Gomperts, R. E. Stratmann, O. Yazyev, A. J. Austin, R. Cammi, C. Pomelli, J. W. Ochterski, R. L. Martin, K. Morokuma, V. G. Zakrzewski, G. A. Voth, P. Salvador, J. J. Dannenberg, S. Dapprich, A. D. Daniels, Ö. Farkas, J. B. Foresman, J. V. Ortiz, J. Cioslowski and D. J. Fox, Gaussian 09, Revision D.01, Gaussian, Inc., Wallingford CT, 2009.

[9] A. D. Becke, *J. Chem. Phys.,* 1993, **98**, 5648.

[10] A. Schäfer, H. Horn and R. Ahlrichs, *J. Chem. Phys.,* 1992, **97**, 2571.

[11] A. Schäfer, C. Huber and R. Ahlrichs, *J. Chem. Phys.,* 1994, **100**, 5829.

[12] J. Tomasi, B. Mennucci and R. Cammi, *Chem. Rev.,* 2005, **105**, 2999.

[13] M. E. Casida and M. Huix-Rotllant, *Annu. Rev. Phys. Chem*., 2012, **63**, 287.

[14] M. E. Casida, C. Jamorski, K. C. Casida and D. R. Salahub, *J. Chem. Phys*., 1998, **108**, 4439.

[15] F. London, *J. Phys. Radium*, 1937, **8**, 397.

[16] R. McWeeny, *Phys. Rev*., 1962, **126**, 1028.

[17] R. Ditchfield, *Mol. Phys*., 1974, **27**, 789.

[18] K. Wolinski and J. F. Hilton, P. Pulay, *J. Am. Chem. Soc*. 1990, 112, 8251.

about the use of the broken-symmetry approach to evaluate the magnetic coupling constants can be found in the literature.[19,20,21,22] A polarizable continuum model (PCM) was introduced in the calculations with the parameters corresponding to acetonitrile.[23] Natural transition orbitals and spin density maps in Figs. 5 and 12 of the manuscript were generated using the VESTA program.[24]

Ab initio calculations of the *zfs* tensors

The parameters that determine the axial (D) and rhombic (E) components of the local zero-field splitting (*zfs*), the g-tensor for the $S = 3/2$ state ($g_{3/2}$) and the ground Kramers doublet (g_{eff}) of **3** and **5** were estimated from theoretical calculations based on a second-order N-electron valence state perturbation theory (CASSCF/NEVPT2) through an effective Hamiltonian for the spin-orbit coupling (SOC),[25,26,27] which often provides accurate values of the nearby excited states energies and for the *zfs* tensor of mononuclear first-row transition metal complexes. Experimental geometries were used in this study. Calculations were carried out on the experimental geometries with version 4.0.1 of the ORCA programme[28] using the def2-TZVP basis set proposed by Ahlrichs[29] and the auxiliary TZV/C Coulomb fitting basis sets.[30,31,32] The contributions to *zfs* from 10 quartet and 20 doublet excited states generated from an active space with seven electrons in five *d* orbitals were included using an effective

[19] E. Ruiz, A. Rodríguez-Fortea, J. Cano, S. Alvarez and P. Alemany, *J. Comput. Chem.*, 2003, **24**, 982-989.

[20] E. Ruiz, J. Cano. S. Alvarez, P. Alemany, *J. Am. Chem. Soc*., 1998, **120**, 11122-11129.

[21] E. Ruiz, P. Alemany, S. Alvarez and J. Cano, *J. Am. Chem. Soc.*, 1997, **119**, 1297-1303.

[22] E. Ruiz, J. Cano, S. Alvarez and P. Alemany, *J. Comput. Chem.*, 1999, **20**, 1391-1400.

[23] J. Tomasi, B. Mennucci and R. Cammi, *Chem. Rev.*, 2005, **105**, 2999-3093.

[24] F. Neese, *The ORCA Program System.* Wires Comput., *Mol. Sci.*, 2012, **2**, 73.

[25] C. Angeli, R. Cimiraglia and J.-P. Malrieu, *Chem. Phys. Lett*., 2001, **350**, 297.

[26] C. Angeli, R. Cimiraglia and J.-P. Malrieu, *J. Chem. Phys*., 2002, **117**, 9138.

[27] C. Angeli, R. Cimiraglia, S. Evangelisti, T. Leininger and J.-P. Malrieu, *J. Chem. Phys*., 2001, **114**, 10252.

[28] K. Momma, F. Izumi, Vesta 3 for three-dimensional visualization of crystal, volumetric and morphology data, *J. Appl. Crystallogr.*, 2011, **44**, 1272.

[29] F. Weigend and R. Ahlrichs, *Phys. Chem. Chem. Phys*., 2005, **7**, 3297.

[30] F. Weigend, *Phys. Chem. Chem. Phys*., 2006, **8**, 1057.

[31] K. Eichkorn, O. Treutler, H. Ohm, M. Haser and R. Ahlrichs, *Chem. Phys. Lett*., 1995, **242**, 652.

[32] K. Eichkorn, F. Weigend, O. Treutler, H. Ohm and R. Ahlrichs, *Theor. Chem. Acc*., 1997, **97**, 119.

Hamiltonian. RIJCOSX method was used combining resolution of the identity (RI) and "chain of spheres" COSX approximations for the Coulomb and exchange terms, respectively.[33,34,35]

[33] F. Neese, F. Wennmohs, A. Hansen and U. Becker, *Chem. Phys*., 2009, **356**, 98.

[34] R. Izsák and F. Neese, *J. Chem. Phys*., 2011, **135**, 144105.

[35] R. Izsák, A. Hansen and F. Neese, *Mol. Phys*., 2012, **110**, 2413.

General characterisation data

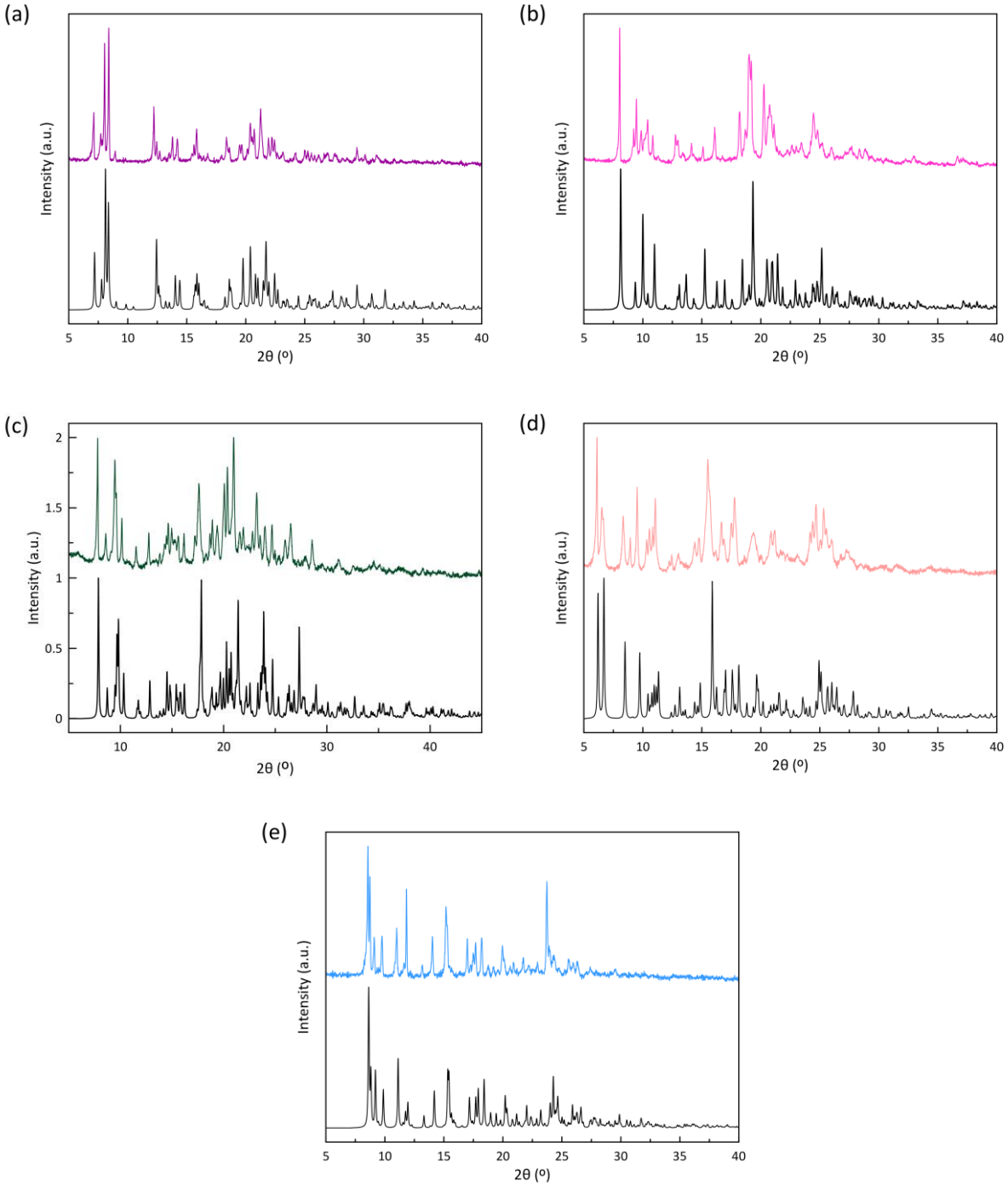

Fig. S1 Powder X-ray diffractograms of **1** (a), **2** (b), **3** (c), **4** (d), and **5** (e). The solid black lines correspond to the calculated X-ray diffractograms.

Structural data

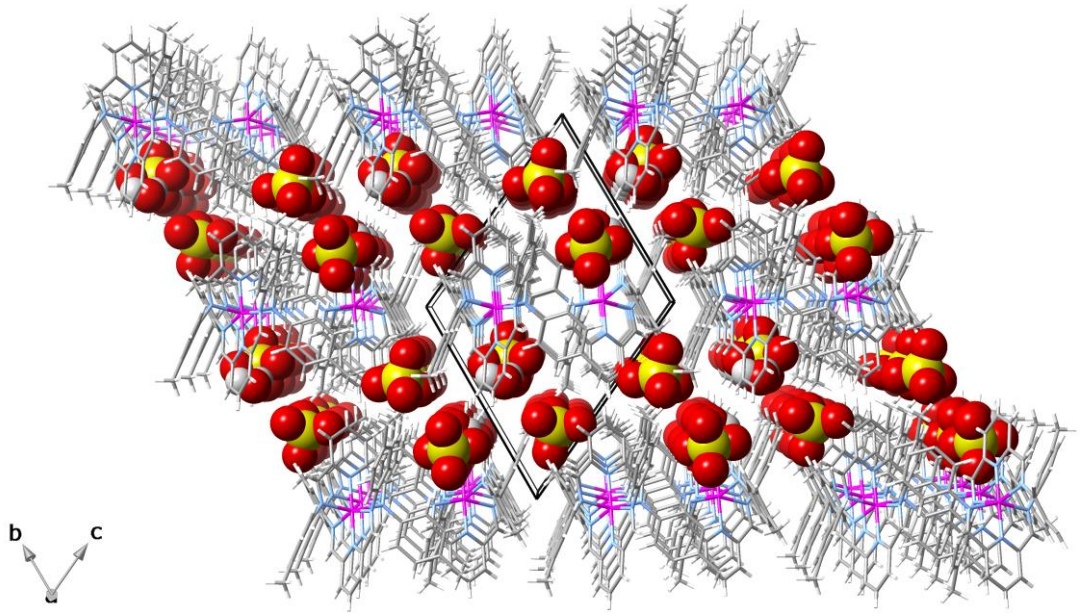

Fig. S2 Perspective view of the crystal packing of **1** along the crystallographic *a* axis. The perchlorate anions and water molecules of crystallisation are shown in a space-filling representation.

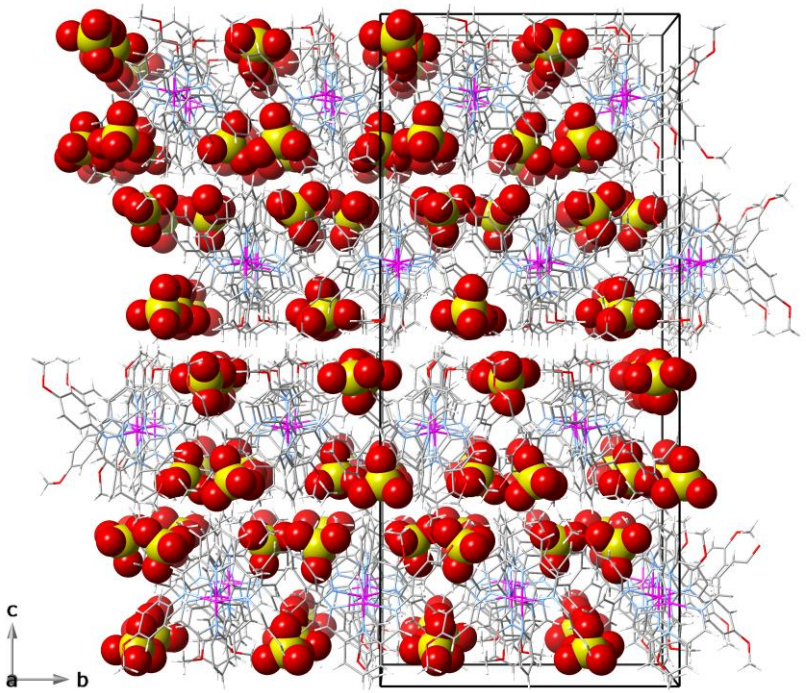

Fig. S3 Perspective view of the crystal packing of **2** along the crystallographic *a* axis. The perchlorate anions are shown in a space-filling representation.

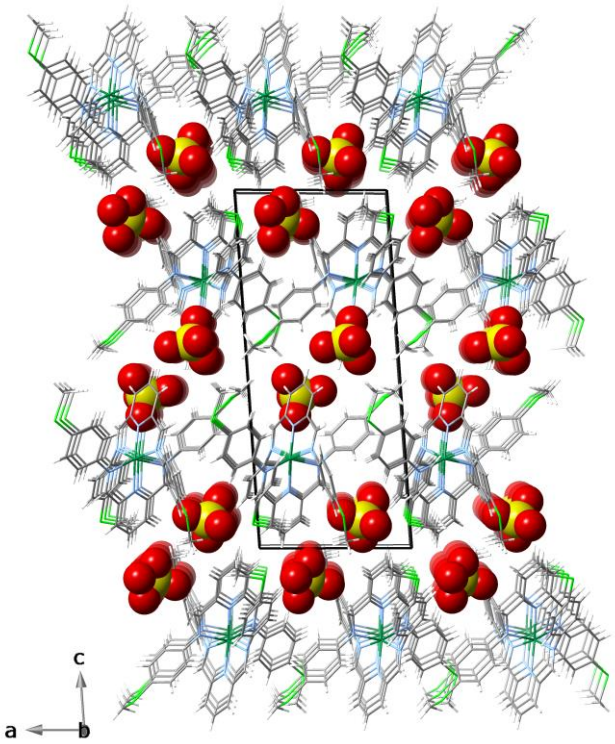

Fig. S4 Perspective view of the crystal packing of **3** along the crystallographic *b* axis. The perchlorate anions are shown in a space-filling representation.

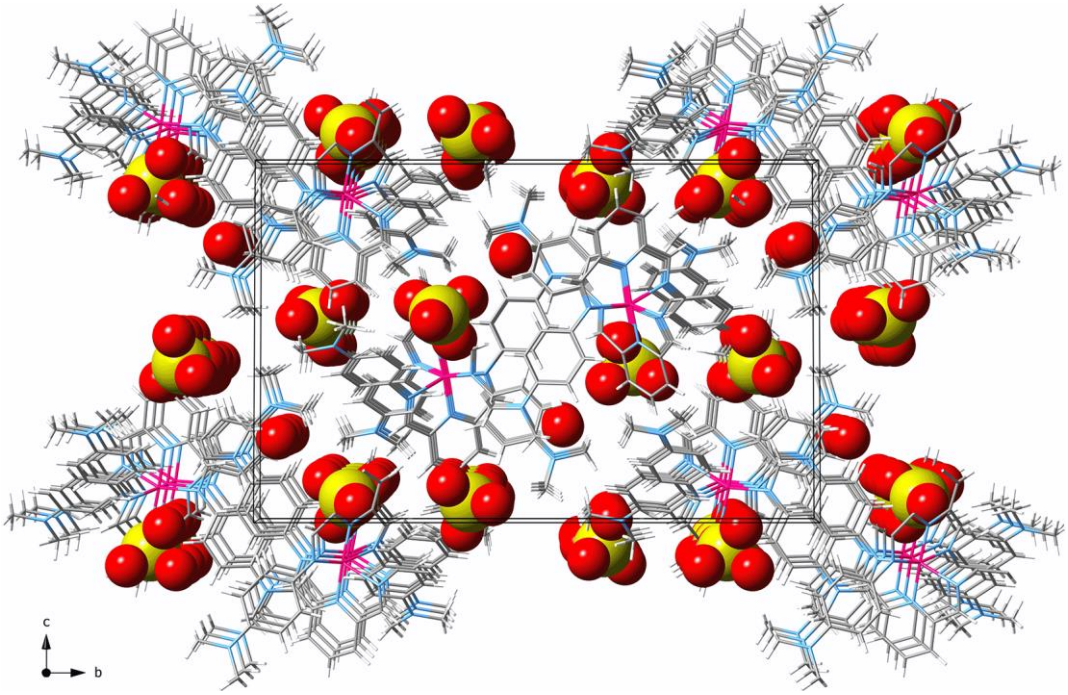

Fig. S5 Perspective view of the crystal packing of **4** along the crystallographic *a* axis. The perchlorate anions and water molecules of crystallisationare shown in a space-filling representation.

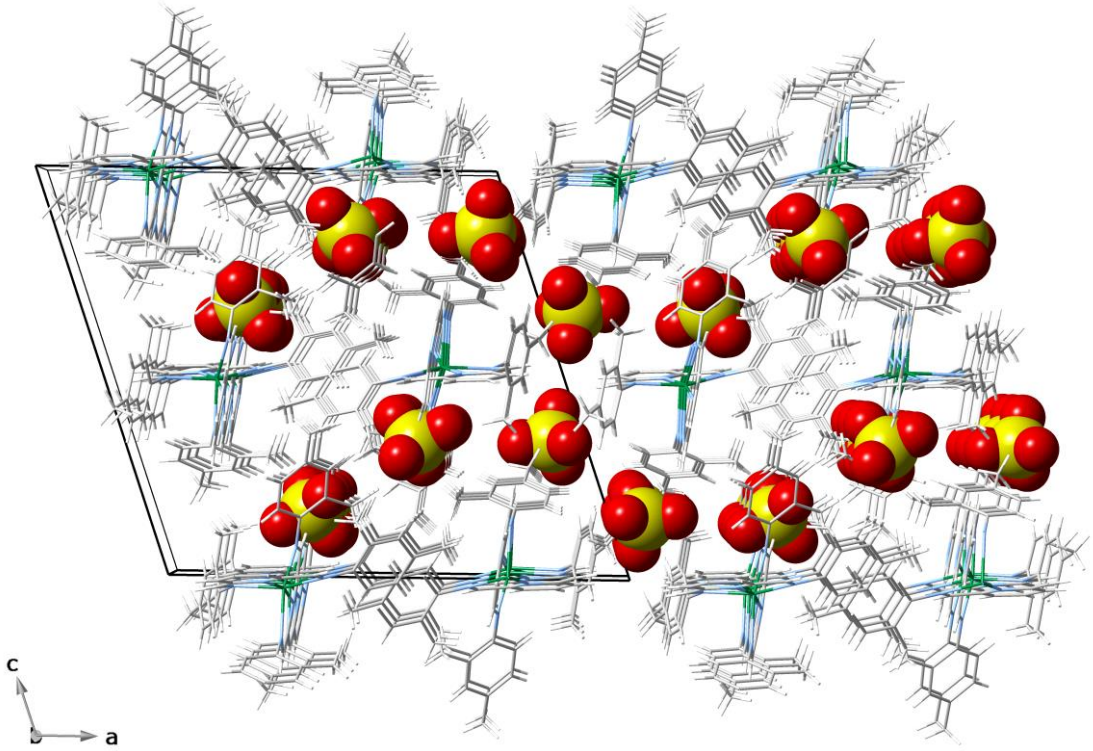

Fig. S6 Perspective view of the crystal packing of **5** along the crystallographic *b* axis. The perchlorate anions are shown in a space-filling representation.

Table S1. Summary of Crystallographic Data for **1**–**5**

	1	**2**	**3**	**4**	**5**
Formula	$C_{42}H_{40}N_6O_9Cl_2Co$	$C_{42}H_{38}N_6O_{12}Cl_2Co$	$C_{42}H_{38}N_6O_8Cl_2CoS_4$	$C_{46}H_{50}N_{10}O_{8.5}Cl_2Co$	$C_{46}H_{46}N_6O_8Cl_2Co$
M (g mol^{-1})	902.63	948.61	1012.85	1008.79	940.72
Crystal system	Triclinic	Tetragonal	Triclinic	Monoclinic	Monoclinic
Space group	*P–1*	*P4₃*	*P–1*	*P2₁/n*	*P2₁/c*
a (Å)	13.3841(9)	19.34260(10)	9.6346(3)	10.6359(3)	20.2948(6)
b (Å)	13.5571(9)	19.34260(10)	10.2111(4)	26.3995(9)	12.1110(5)
c (Å)	13.5951(9)	43.5392(5)	22.5333(8)	17.1889(6)	18.9256(7)
α (°)	64.786(6)	90	88.0330(10)	90	90
β (°)	83.381(5)	90	85.7490(10)	99.6030(10)	108.743(4)
γ (°)	67.121(6)	90	82.9460(10)	90	90
V (Å^3)	2052.5(3)	16289.6(3)	2193.28(13)	4758.7(3)	4405.05(5)
Z	2	16	2	4	4
ρ_{calc} (g cm^{-3})	1.461	1.547	1.534	1.408	1.418
μ (mm^{-1})	5.014	0.627	0.764	0.538	4.678
T (K)	100	150	150	150	100
Reflect. collcd.	8104	36206	16740	11787	8636
Reflect. obs. [$I > 2\sigma(I)$]	6894	30594	13706	7966	7275
Data	8104	36206	16740	11787	8636
Parameters	551	2286	585	701	576
Restraints	0	1	58	294	0
R_1[a] [$I > 2\sigma(I)$]	0.0471	0.0505	0.0402	0.0608	0.0481
wR_2[b] [$I > 2\sigma(I)$]	0.1187	0.1135	0.0947	0.1396	0.1188
S[c]	1.036	0.978	1.063	1.040	1.027

[a] $R_1 = \sum(|F_o| - |F_c|)/\sum|F_o|$. [b] $wR_2 = [\sum w(F_o^2 - F_c^2)^2/\sum w(F_o^2)^2]^{1/2}$. [c] $S = [\sum w(|F_o| - |F_c|)^2/(N_o - N_p)]^{1/2}$.

Table S2. Selected Structural Data for **1**–**5**[a]

	1	**2**	**3**	**4**	**5**
R_1(Co–N_{im})[b] (Å)	2.206(2)	2.085(4)/2.180(4)/2.090(4)/2.185(4)	2.217(2)	2.196(3)	2.215(2)
R_2(Co–N'$_{im}$)[b] (Å)	2.029(2)	2.085(4)/2.114(4)/2.076(4)/2.096(4)	2.186(2)	2.033(3)	2.156(2)
R_3(Co–N_{py})[c] (Å)	1.896(3)	1.872(5)/1.905(5)/1.874(5)/1.902(5)	2.047(2)	1.885(2)	2.018(2)
R_{eq}[d] (Å)	2.118(2)	2.085(4)/2.147(4)/2.083(4)/2.141(4)	2.202(2)	2.115(3)	2.186(2)
δ_R[e]	0.084(2)	0.000(4)/0.031(4)/0.007(4)/0.042(4)	0.014(2)	0.077(3)	0.027(2)
R[f] (Å)	2.043(3)	2.014(5)/2.066(5)/2.013(5)/2.061(5)	2.150(2)	2.038(3)	2.130(2)
Δ_R[g]	0.108(3)	0.106(5)/0.117(5)/0.103(5)/0.115(5)	0.072(2)	0.113(4)	0.079(2)
N_{im}–Co–N'$_{im}$[h] (°)	87.73(9)	84.1(2)/92.0(2)/84.2(2)/92.1(2)	89.7(4)	83.21(10)	88.82(9)
N'$_{im}$–Co–N_{im}[h] (°)	96.45(9)	100.1(2)/92.6(2)/100.0(2)/92.4(2)	98.5(4)	101.08(10)	98.52(8)
N_{py}–Co–N_{py}[i] (°)	176.1(1)	177.4(2)/176.6(2)/178.4(2)/178.5(2)	164.3(4)	177.06(11)	162.38(9)
δ[j] (Å)	±0.407	±0.395/±0.430/±0.395/±0.421	±0.560	±0.409	±0.555
Φ[k] (°)	81.74(2)	72.24(2)/89.88(2)/72.72(2)/89.97(2)	80.42(4)	73.97(4)	79.33(2)
φ[l] (°)	41.41(4)	43.7(8)/41.3(8)/44.5(8)/40.5(8)	46.1(4)	37.7(4)	63.3(4)
d_0(C_{ph}–N_{im})[m] (Å)	1.431(4)	1.425(7)/ 1.424(7)/ 1.420(7)/ 1.422(7)	1.423(3)	1.420(4)	1.432(3)
d_1(C_{py}–N_{py})[n] (Å)	1.349(4)	1.347(7)/ 1.345(7)/ 1.347(7)/ 1.345(7)	1.337(3)	1.347(4)	1.338(3)
d_2(C_{py}–C_{im})[o] (Å)	1.465(4)	1.459(8)/ 1.454(8)/ 1.466(8)/ 1.453(8)	1.467(3)	1.455(4)	1.474(4)
d_3(C_{im}–N_{im})[p] (Å)	1.282(4)	1.288(7)/ 1.289(7)/ 1.287(7)/ 1.291(7)	1.285(3)	1.289(4)	1.276(3)
Δ_d[q] (Å)	0.1495(4)	0.1415(7)/ 0.1370(7)/ 0.1490(7)/ 0.1350(7)	0.156(3)	0.137(4)	0.1670(3)
h[r] (Å)	3.716	3.839/4.273/3.938/4.502	3.760 3.828	4.202	3.614
θ[s] (°)	26.76	26.17/49.58/29.42/59.14	19.50 26.15	47.77	17.76

[a] Structural data for each crystallographically independent cobalt atom. [b] Average cobalt-nitrogen imine equatorial bond distances from each PDI ligand. [c] Average cobalt-pyridine nitrogen axial bond distances from the two PDI ligands. [d] Average cobalt-nitrogen equatorial bond distances defined as $R_{eq} = (R_1 + R_2)/2$. [e] Rhombic distortion parameter defined as $\delta_R = (R_1 - R_2)/R_{eq}$. [f] Average cobalt-nitrogen bond distances defined as $R = (R_1 + R_2 + R_3)/3$. [g] Axial distortion parameter defined as $\Delta_R = (R_{eq} - R_{ax})/R$. [h] Average cobalt-nitrogen imine equatorial bond angles from the two PDI ligands. [i] Cobalt-nitrogen pyridine axial bond angle from the two PDI ligands. [j] Mean deviations of the imine nitrogen donor atoms from the metal equatorial plane. [k] Dihedral angle between the mean planes of the pyridinediimine fragments from the two PDI ligands. [l] Average torsional angle for the phenylimine ligand fragments from each PDI ligand. [m] Average phenyl carbon-imine nitrogen bond distance from the phenylimine ligand fragment. [n] Average pyridine carbon-pyridine nitrogen bond distance from the pyridinediimine ligand fragment. [o] Average pyridine carbon-imine carbon bond distance from the pyridinediimine ligand fragment. [p] Average imine carbon-nitrogen bond distance from the pyridinediimine ligand fragment. [q] Alternance bond parameter for the pyridinediimine ligand fragment defined as $\Delta_d = d_2 - (d_1 + d_3)/2$. [r] Intramolecular distance between the centroids of the pyridine and phenyl rings from the two PDI ligands. [s] Dihedral angle between the mean planes of the pyridine and phenyl rings from the two PDI ligands.

Structural and spectroscopic correlations

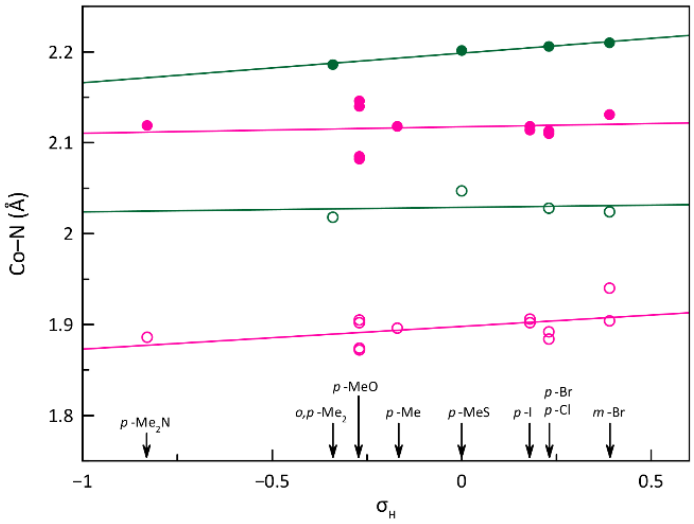

Fig. S7 Variation of the R_{eq} (●) and R_3 (**O**) values for each crystallographically independent cobalt atom with the Hammett constants (σH) of the ligand substituents for **1**–**9** (data taken from Table S2 and ref. 1). The structural data for the HS and LS Co^{II} ions are drawn in green and pink colours, respectively. The identity of the ligand substituents is included for clarity. The solid lines are the linear fit curves (see text).

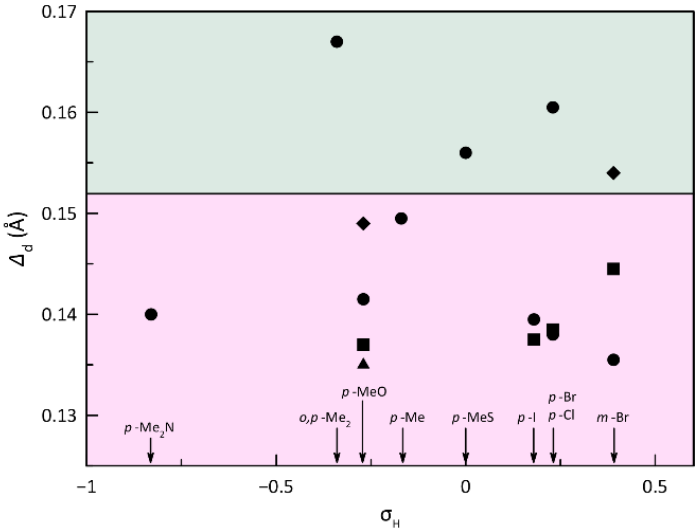

Fig. S8 Variation of the Δ_d values for each crystallographically independent cobalt atom with the Hammett constants (σ_H) of the ligand substituents for **1**–**9** (data taken from Table S2 and ref. 1). The identity of the ligand substituents is included. Distinct symbols are used for crystallographically independent Co(II) complex units.

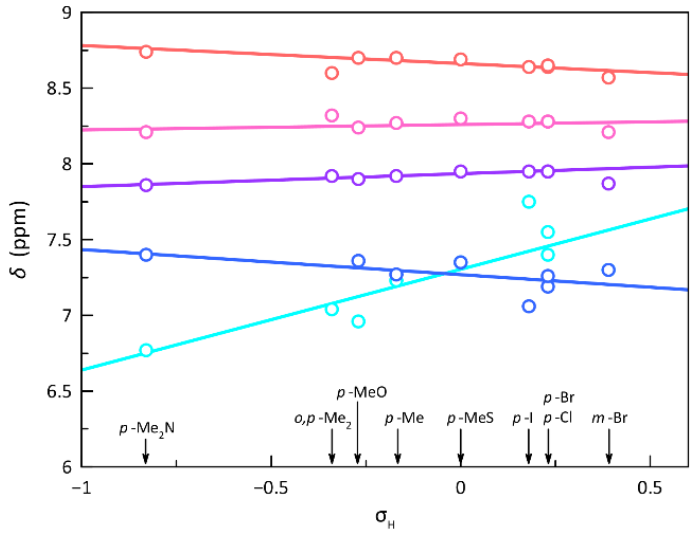

Fig. S9 Variation of the chemical shift (δ) values with the Hammett constants (σ_H) of the ligand substituents for the imine (red), para- (pink) or meta- (purple) pyridine, and ortho/para- (blue), meta- (cyan) phenyl protons from the PDI ligands. The identity of the ligand substituents is included for clarity. The solid lines are the linear fit curves (see text).

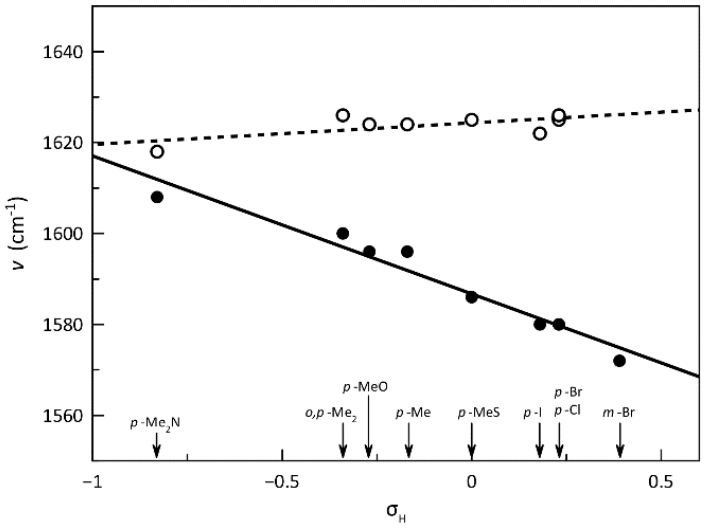

Fig. S10 Variation of the energy values of the ν(C=N) imine stretching vibration for the PDI ligands (**O**) and the corresponding cobalt(II) complexes **1**–**9** (●) with the Hammett constants (σ_H) of the ligand substituents. The identity of the ligand substituents is included for clarity. The dashed and solid lines are the linear fit curves for the ligands and complexes, respectively (see text).

Theoretical calculations

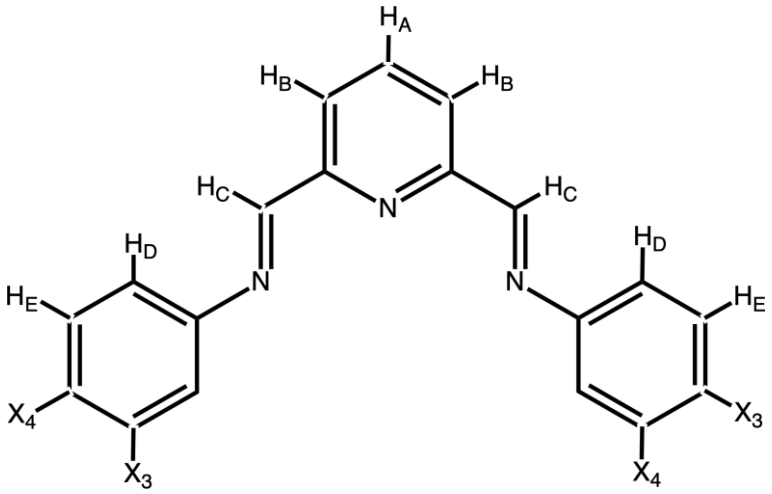

Scheme S1. Chemical formula of PDI ligand showing labelled hydrogen nucleus.

Table S3. Calculated ^{1}H NMR chemical shifts (δ, in ppm) for hydrogen nucleus, labelled according to Scheme S1, in the optimised geometries of 4-MePhPDI, 4-Me_2NPhPDI, 2,4-Me_2PhPDI ligands, and 4-MePhPDI built by removing 2-Me groups from the 2,4-Me_2PhPDI in its optimised geometries (4-MePhPDI*)

H site	δ (4-MePhPDI)	δ (4-Me_2NPhPDI)	δ (2,4-Me_2PhPDI)	δ (4-MePhPDI*)
H_A	8.23	8.07	8.23	8.23
H_B	7.78	7.56	7.79	7.79
H_C	8.71	8.87	8.60	8.60
H_D	7.32	7.70	7.09	7.08
H_E	7.46	6.75	7.28	7.42

Table S4. Calculated wavelengths (in nm) for the main electronic transitions on the optimised geometries of the 4-MePhPDI and 4-Me_2NPhPDI ligands and that of the latter in the conformation adopted in the optimised geometry of its cobalt(II) complex **4**

Electronic transition	4-MePhPDI	4-Me_2NPhPDI	4-Me_2NPhPDI in **4**
λ_3, n-π*	385	479	529
$\lambda_{2,2'}$, n-π*	339	419/411	468
λ_1, π-π*	288	287	350
π-π*	245	263	299
π-π*	237	244	276

Spectroscopic properties

Table S5. Best parameters for simulation of the LS contribution in the Q-band EPR spectra of **1**–**5** from the experimental data in solid state at 4.0 K

	g_x	g_y	g_z	g^a
1	2.029	2.116	2.237	2.129
2	2.053	2.053	2.233	2.115
3	-	-	-	-
4	2.034	2.066	2.249	2.118
5	2.182	2.182	2.010	2.126

[a] Overall g value estimated by the equation $g^2 = (g_x^2 + g_y^2 + g_z^2)/3$.

Magnetic properties

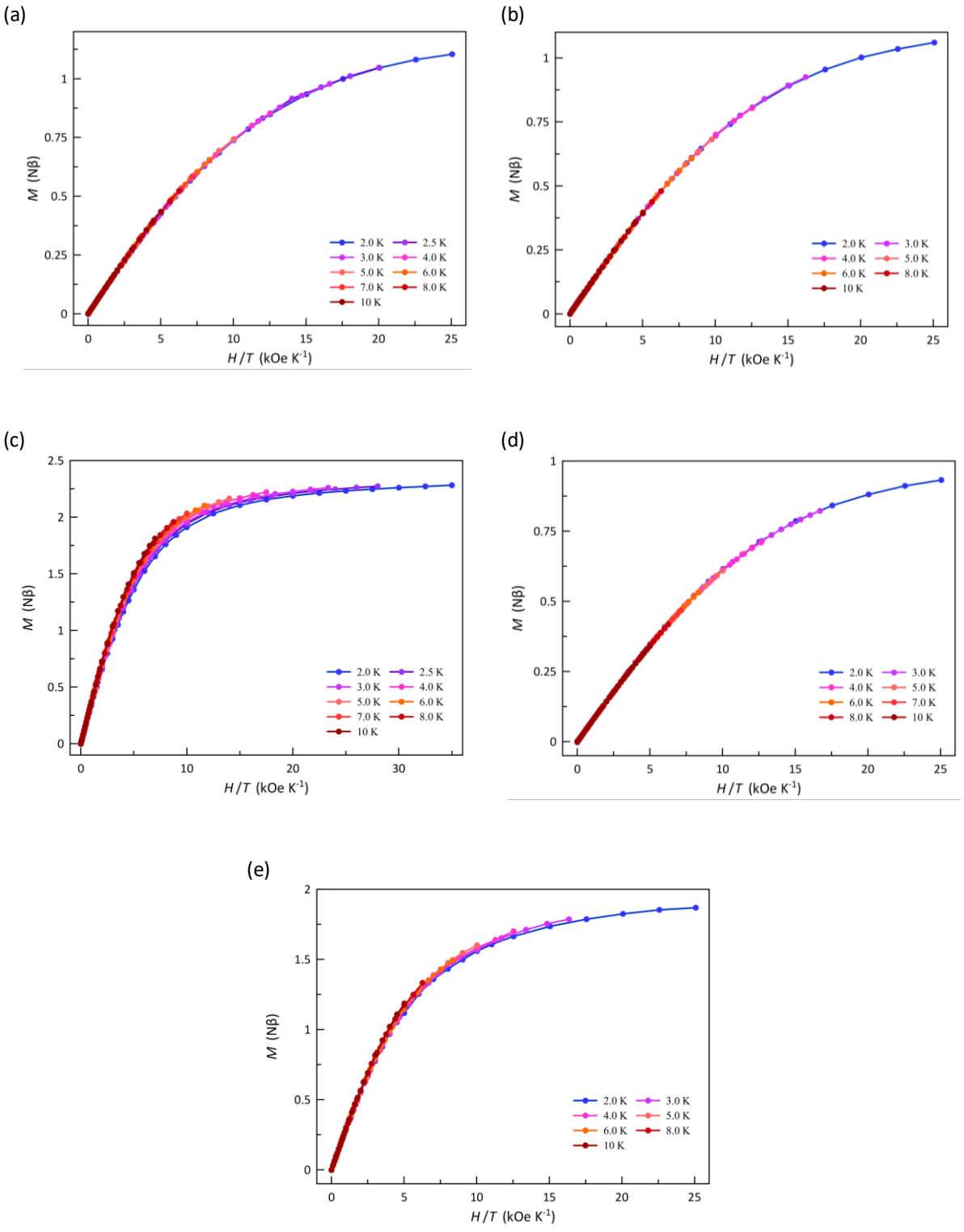

Fig. S11 *M* vs *H*/*T* plots for **1** (a), **2** (b), **3** (c), **4** (d), and **5** (e) in the temperature range of 2.0–10 K. The solid lines are only eye-guides.

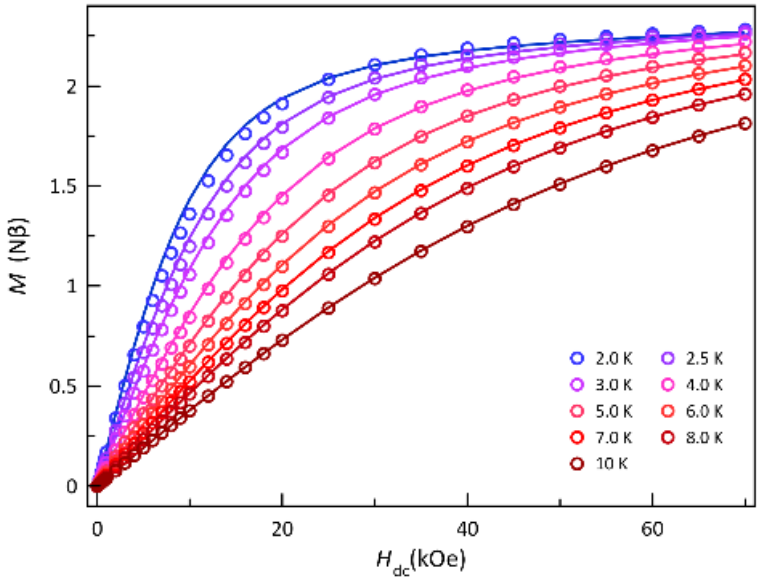

Fig. S12 Field dependence of *M* curves for **3** in the range 2.0–10 K: experimental (O); best-fit curves (–) to the experimental data (see text).

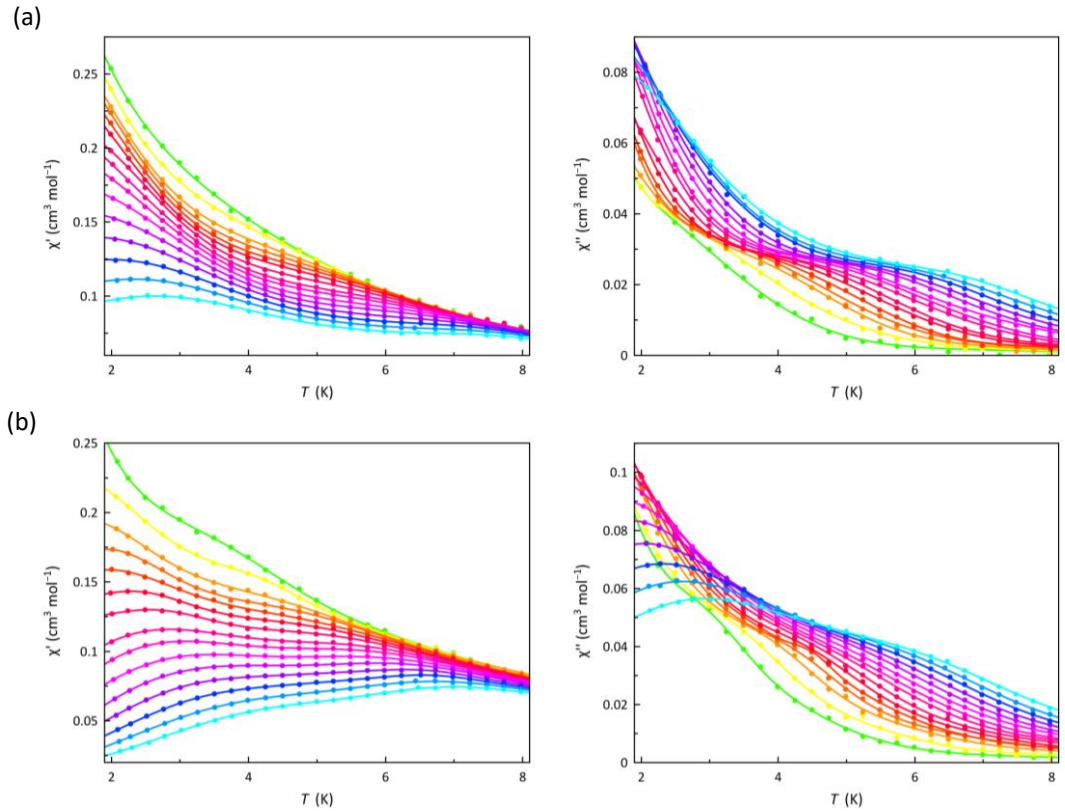

Fig. S13 Temperature dependence of χ_M' (left) and χ_M'' (right) for **1** at a ±5.0 G oscillating field in the frequency range of 0.3–10.0 kHz (green to cyan) under applied static magnetic fields of 1.0 (a) and 2.5 kOe (b). The solid lines are only eye-guides.

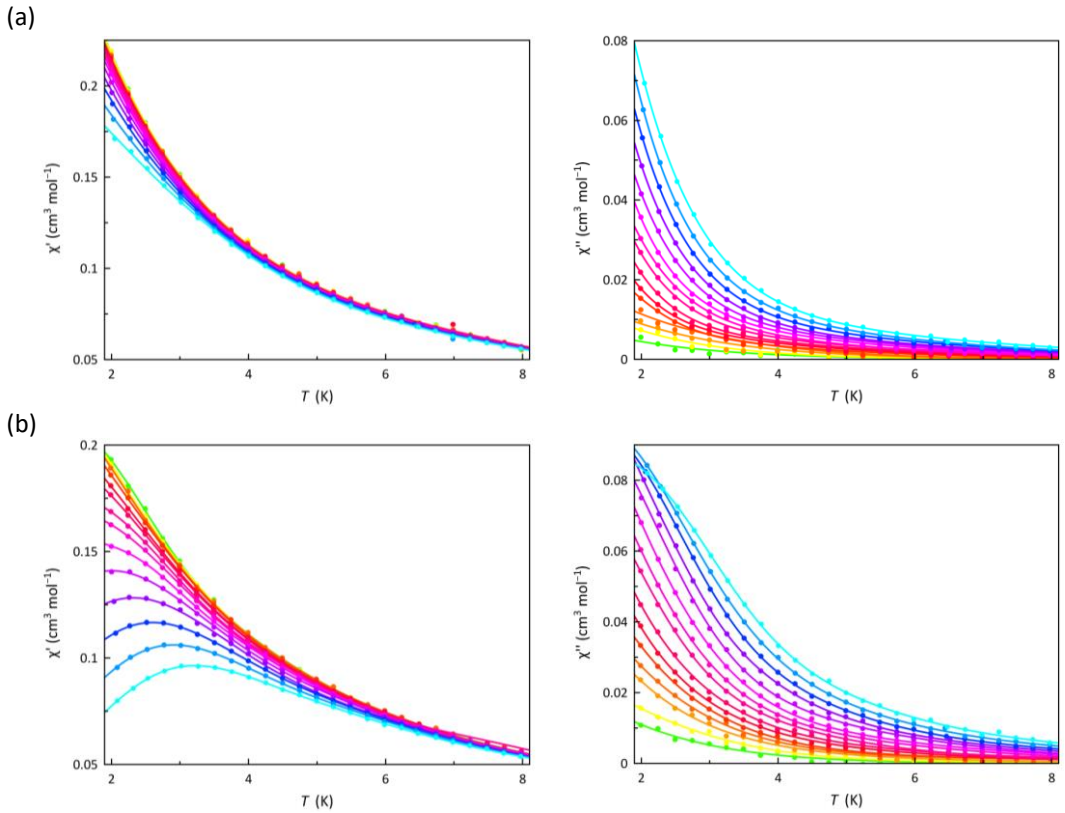

Fig. S14 Temperature dependence of χ_M' (left) and χ_M'' (right) for **2** at a ±5.0 G oscillating field in the frequency range of 0.3–10.0 kHz (green to cyan) under applied static magnetic fields of 1.0 (a) and 2.5 kOe (b). The solid lines are only eye-guides.

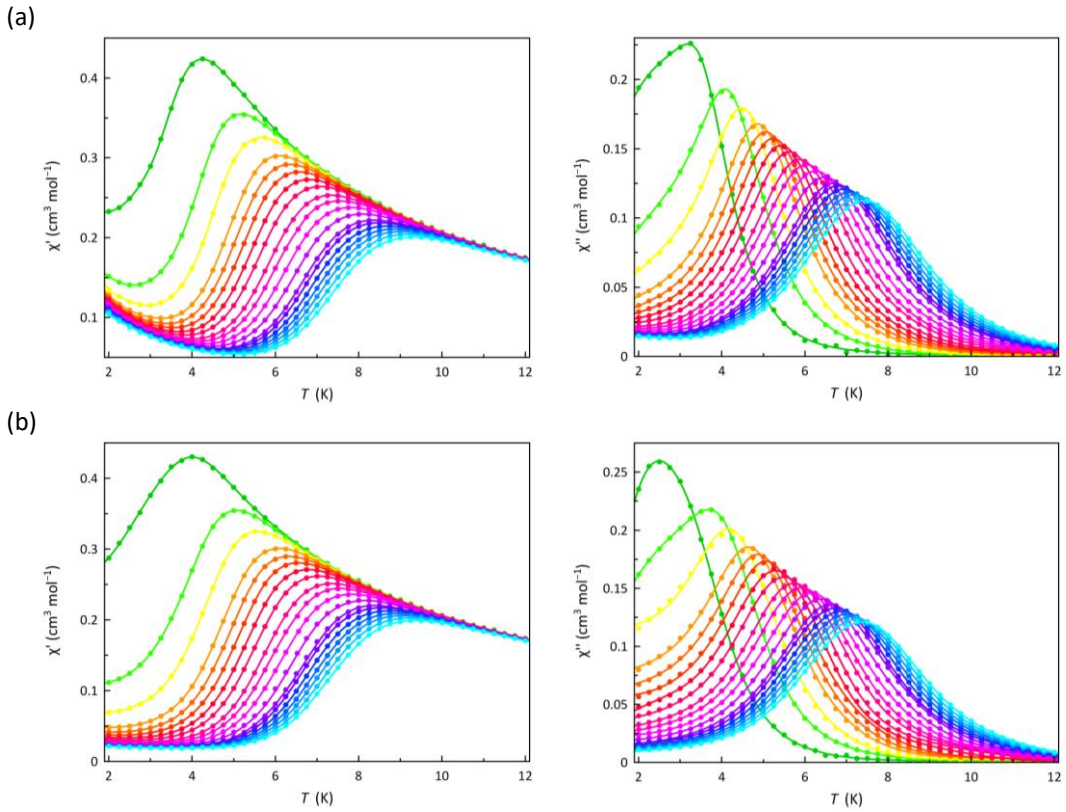

Fig. S15 Temperature dependence of χ_M' (left) and χ_M'' (right) for **3** at a ±5.0 G oscillating field in the frequency range of 0.3–10.0 kHz (green to cyan) under applied static magnetic fields of 1.0 (a) and 2.5 kOe (b). The solid lines are only eye-guides.

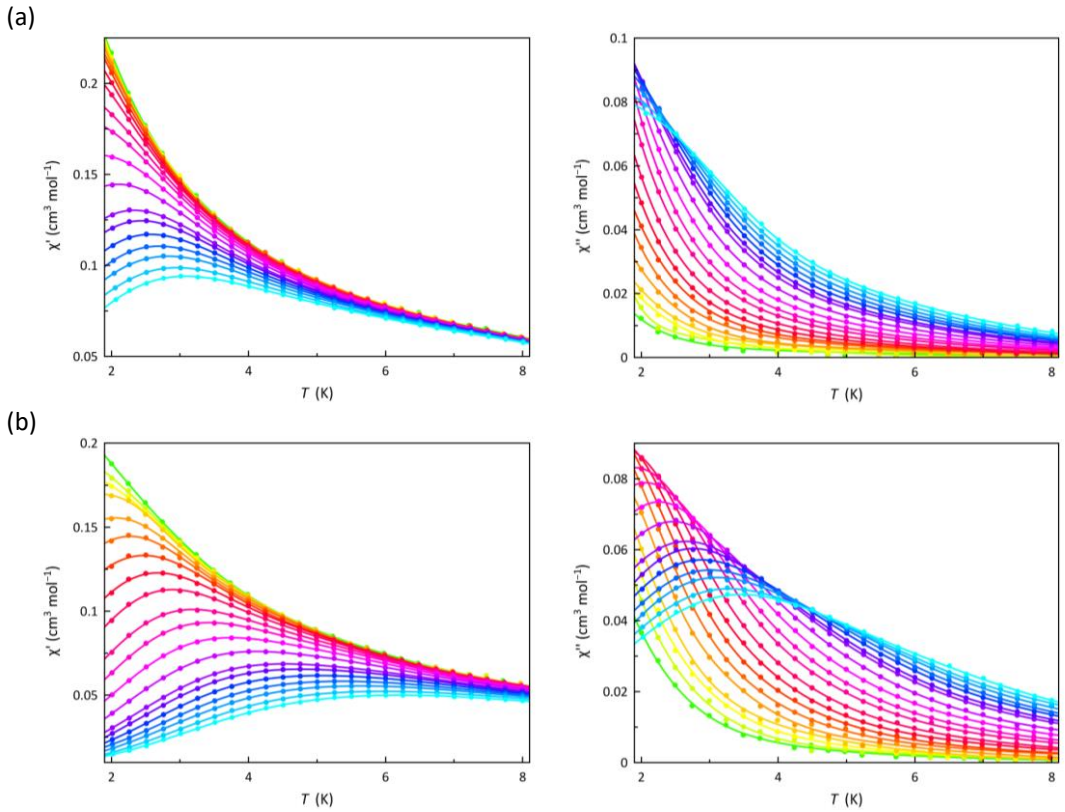

Fig. S16 Temperature dependence of χ_M' (left) and χ_M'' (right) for **4** at a ±5.0 G oscillating field in the frequency range of 0.3–10.0 kHz (green to cyan) under applied static magnetic fields of 1.0 (a) and 2.5 kOe (b). The solid lines are only eye-guides.

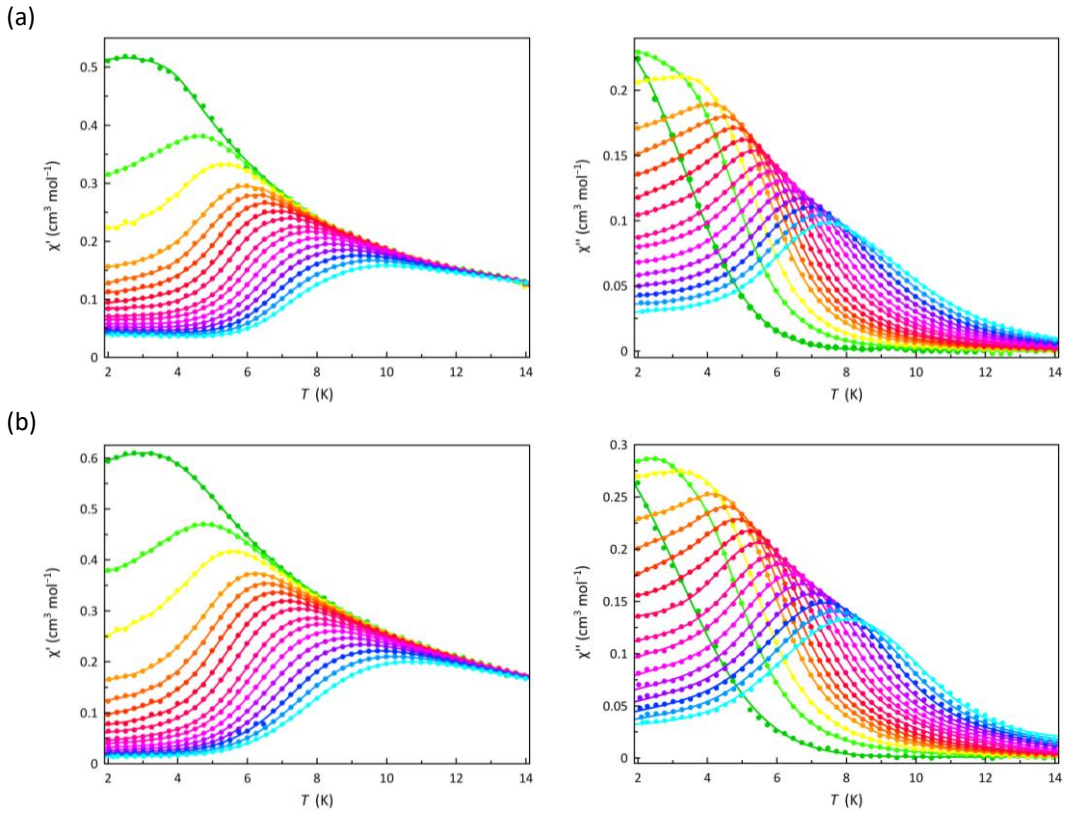

Fig. S17 Temperature dependence of χ_M' (left) and χ_M'' (right) for **5** at a ±5.0 G oscillating field in the frequency range of 0.3–10.0 kHz (green to cyan) under applied static magnetic fields of 1.0 (a) and 2.5 kOe (b). The solid lines are only eye-guides.

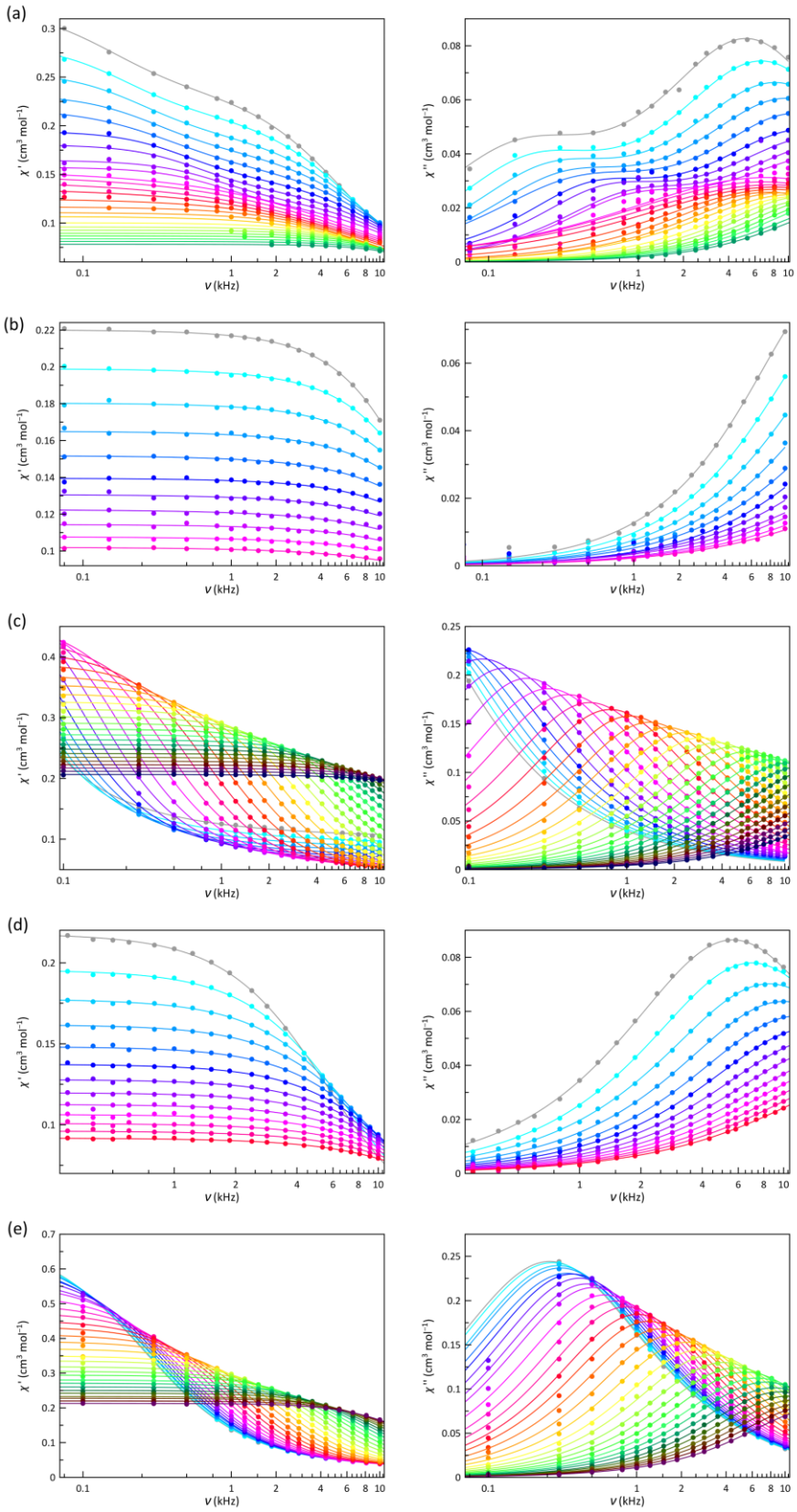

Fig. S18 Frequency dependence of χ_M' (left) and χ_M'' (right) for **1** (a), **2** (b), **3** (c), **4** (d), and **5** (e) at a ±5.0 G oscillating field in the temperature range of 2.0–10 K under an applied static magnetic field of 1.0 kOe. The solid lines are the best fit curves simulated by using the generalised Debye model (see text).

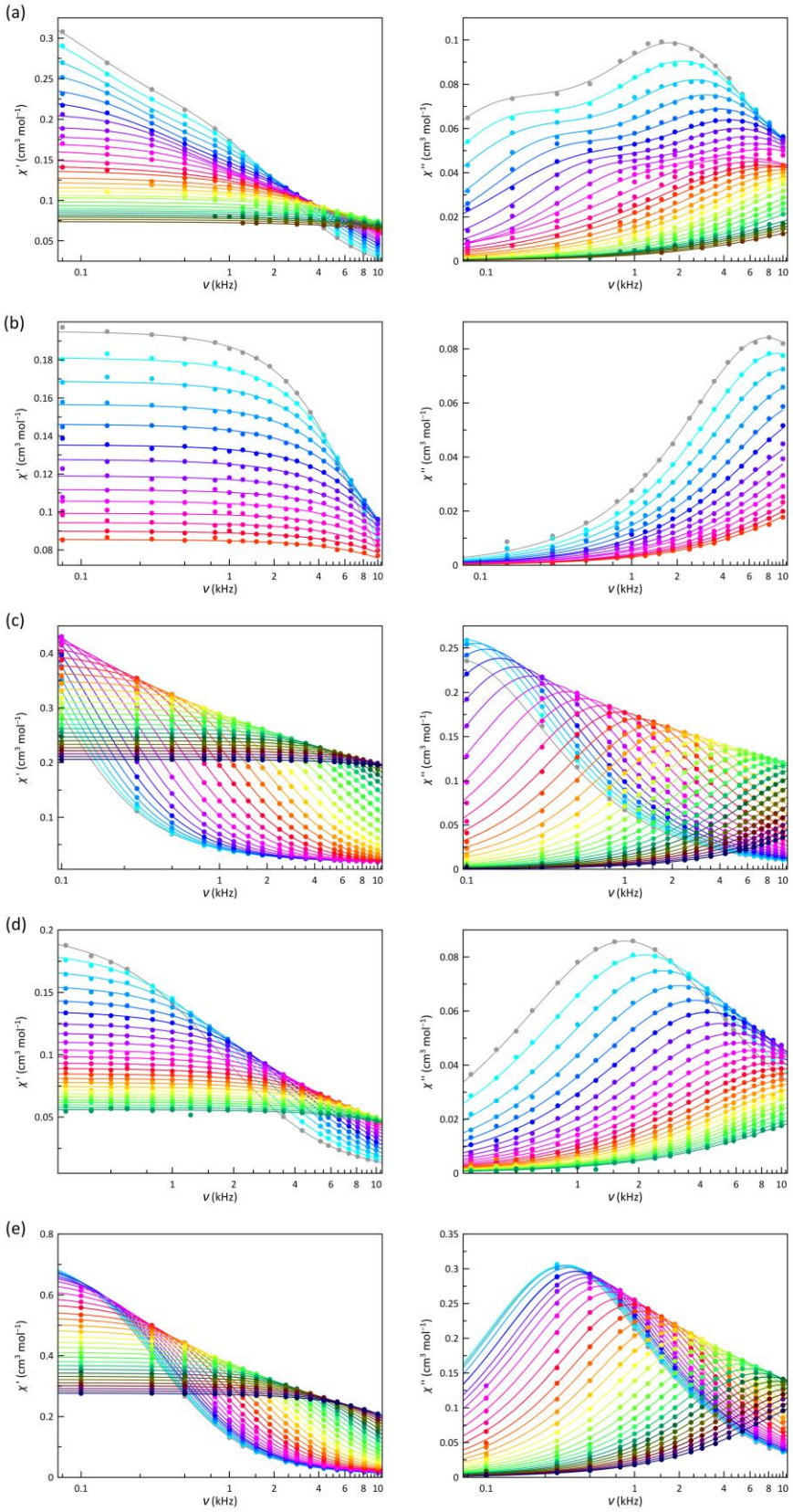

Fig. S19 Frequency dependence of χ_M' (left) and χ_M'' (right) for **1** (a), **2** (b), **3** (c), **4** (d), and **5** (e) at a ±5.0 G oscillating field in the temperature range of 2.0–10 K under an applied static magnetic field of 2.5 kOe. The solid lines are the best fit curves simulated by using the generalised Debye model (see text).

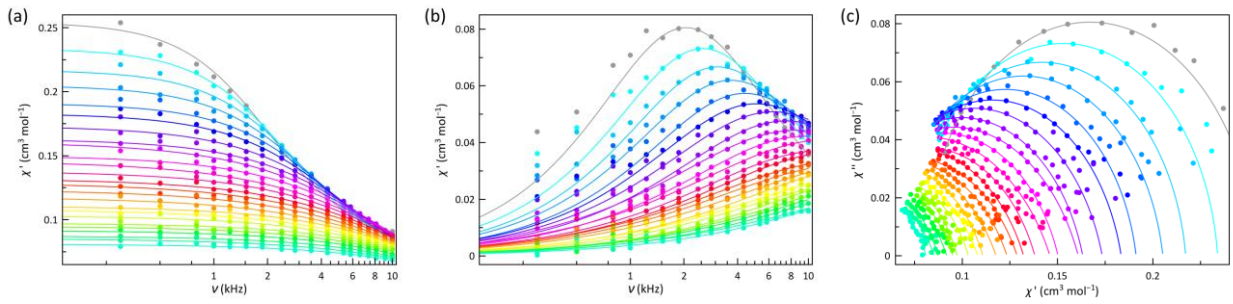

Fig. S20 Frequency dependence of χ_M' (a) and χ_M'' (b) and Argand plots (c) for **2** in frozen acetonitrile at a ±5.0 G oscillating field in the temperature range of 2.0–8.0 K under an applied static magnetic field of 2.5 kOe. The solid lines are the best fit curves simulated by using the generalised Debye model (see text).

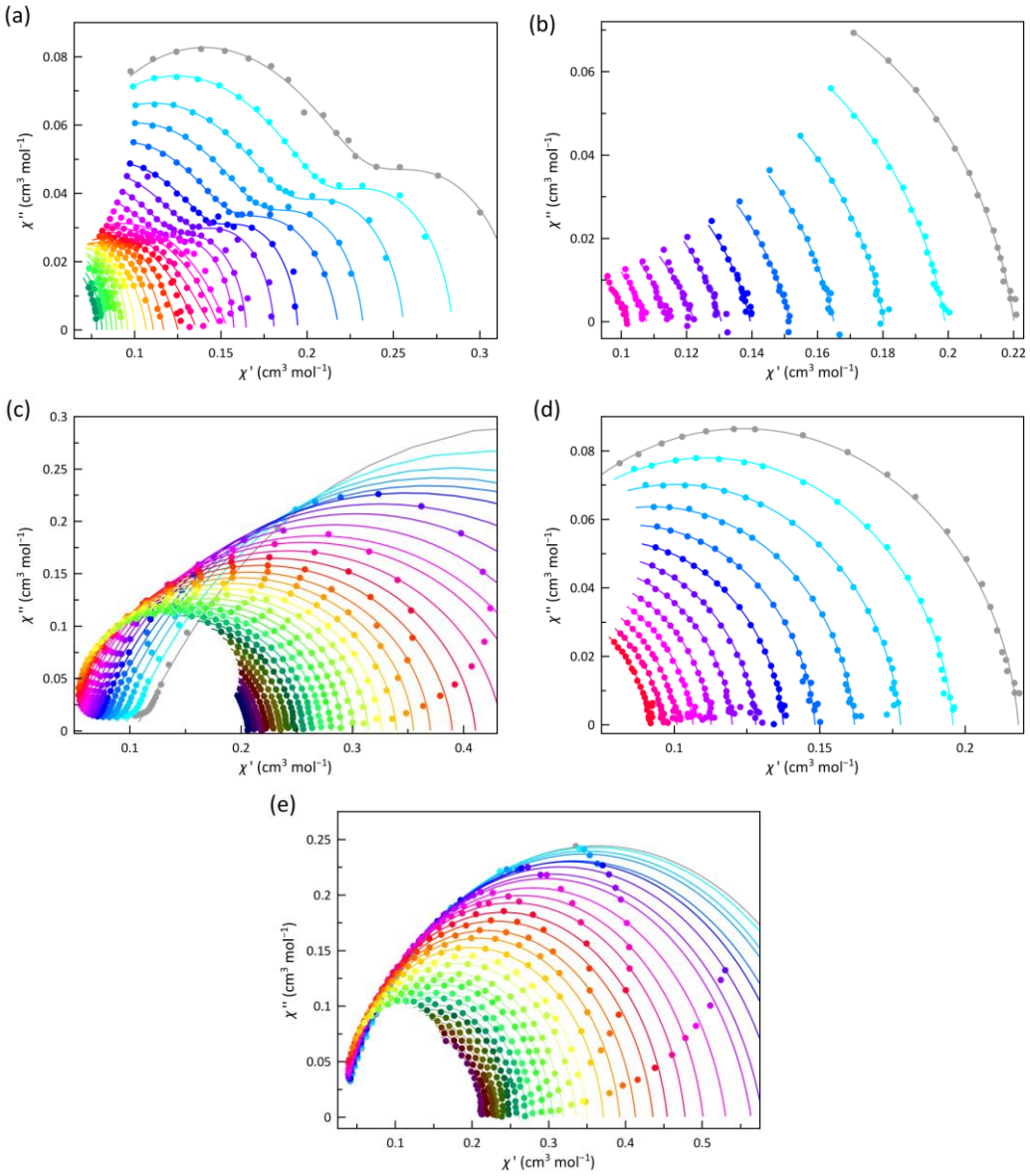

Fig. S21 Argand plots for the calculated magnetic relaxation times (τ) of **1**–**5** (a–e) under an applied *dc* magnetic field of 1.0 kOe. The solid lines are the simulated curves by using the best-fit parameters obtained through the fitting of the χ_M' and χ_M'' *vs* ν plots by the generalised Debye model.

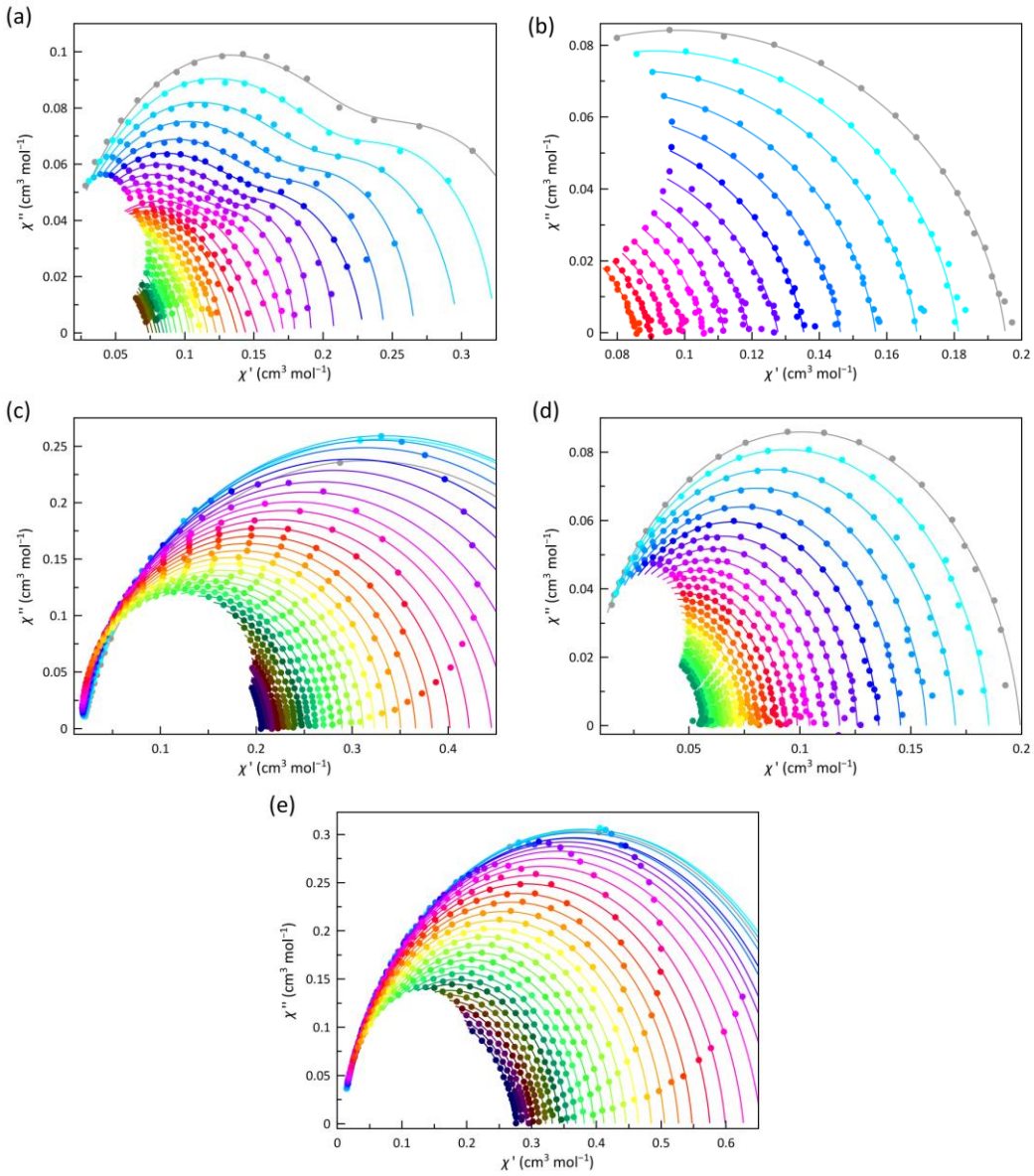

Fig. S22 Argand plots for the calculated magnetic relaxation times (τ) of **1**–**5** (a–e) under an applied *dc* magnetic field of 2.5 kOe. The solid lines are the simulated curves by using the best-fit parameters obtained through the fitting of the χ_M' and χ_M'' *vs* ν plots by the generalised Debye model.

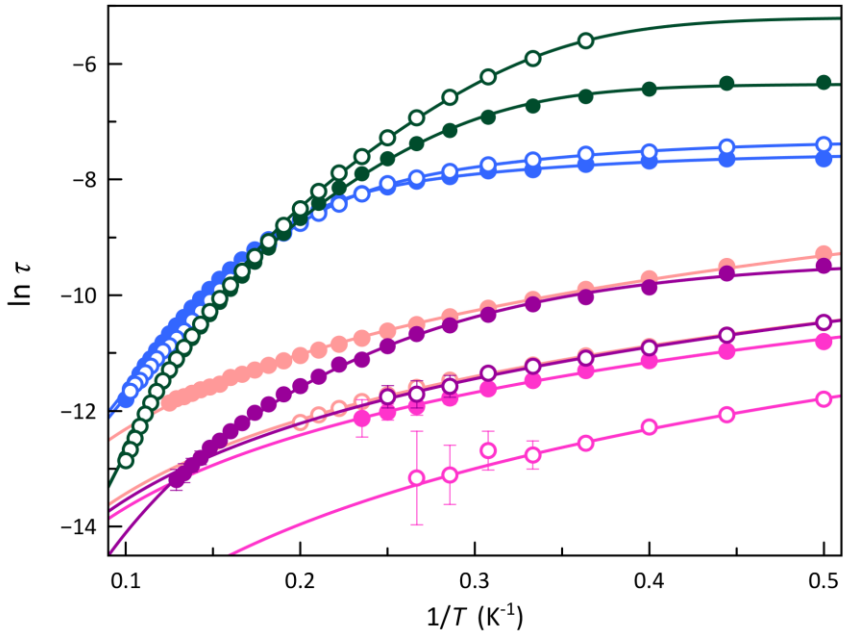

Fig. S23 Arrhenius plots for **1** (purple), **2** (pink), **3** (green), **4** (pale pink) and **5** (blue) under applied *dc* magnetic fields of 1.0 (○), 2.5 (●). The solid and dashed lines are the best-fit curves (see text). Vertical error bars denote the standard deviations.

Table S6. Selected parameters from the least-squares fit of the ac magnetic data of **1**–**5**[a]

	H_{dc} (kOe)	τ_{IK}[b] (x 10^{-3} s)	C[c] ($s^{-1}K^{-n}$)	n[c]
1	1.0	-	9100 ± 500	1.94 ± 0.05
	2.5	0.091 ± 0.004	230 ± 20	3.75 ± 0.06
			78 ± 4	2.81 ± 0.04
2	1.0	-	25400 ± 1300	2.37 ± 0.05
	2.5	0.061 ± 0.013	6900 ± 1200	2.23 ± 0.11
3	1.0	7.39 ± 0.16	0.332 ± 0.007	5.959 ± 0.011
	2.5	1.81 ± 0.05	0.40 ± 0.03	5.91 ± 0.04
4	1.0	-	10000 ± 180	1.818 ± 0.015
	2.5	-	3010 ± 50	1.875 ± 0.010
5	1.0	0.610 ± 0.014	1.9 ± 0.2	4.88 ± 0.05
	2.5	0.485 ± 0.003	1.33 ± 0.07	4.97 ± 0.03

[a] The fits correspond to simple or double relaxation models. [b] Coefficient factor for the temperature-independent *IK* process ($\tau^{-1} = \tau_{IK}^{-1}$). [c] Coefficient and polynomial factor for the Raman process ($\tau^{-1} = CT^n$).

Magnetic correlations

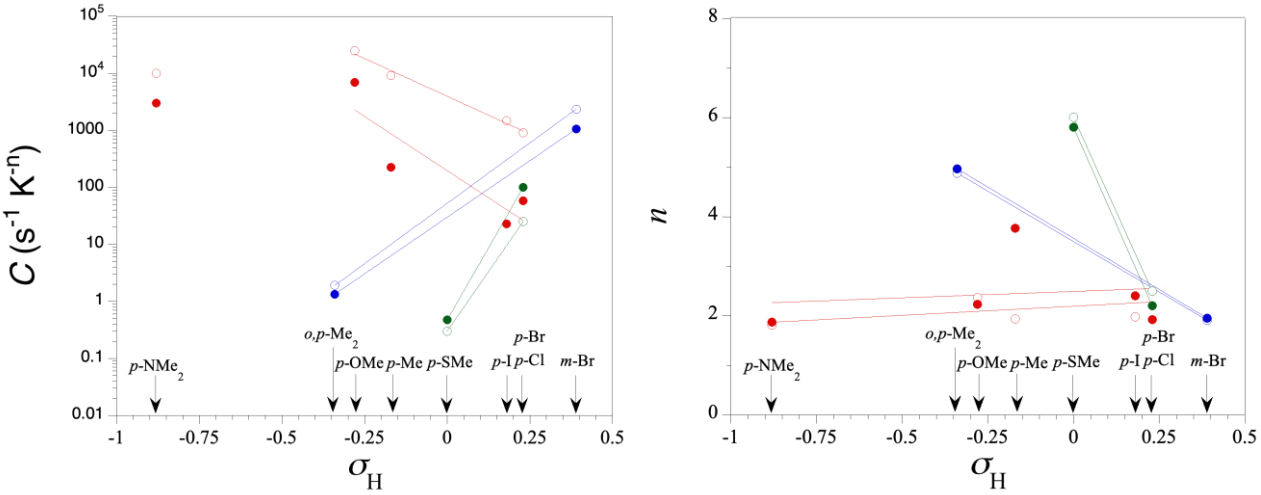

Fig. S24 Variation of the calculated values of *C* (a) and *n* (b) for the Raman relaxation mechanism under applied dc magnetic fields of 1.0 (○) and 2.5 kOe (●) for the cobalt(II)-PDI complexes **1**–**9** with the Hammett constants (σ_H) of the ligand substituents. The identity of the ligand substituents is included for clarity. The magnetic relaxation data for the LS, HS, and LS/HS complexes are drawn in red, green, and blue colours, respectively. Solid lines are the best-fit exponential (a) and linear (b) curves (see text).

Electrochemical properties and magnetic couplings

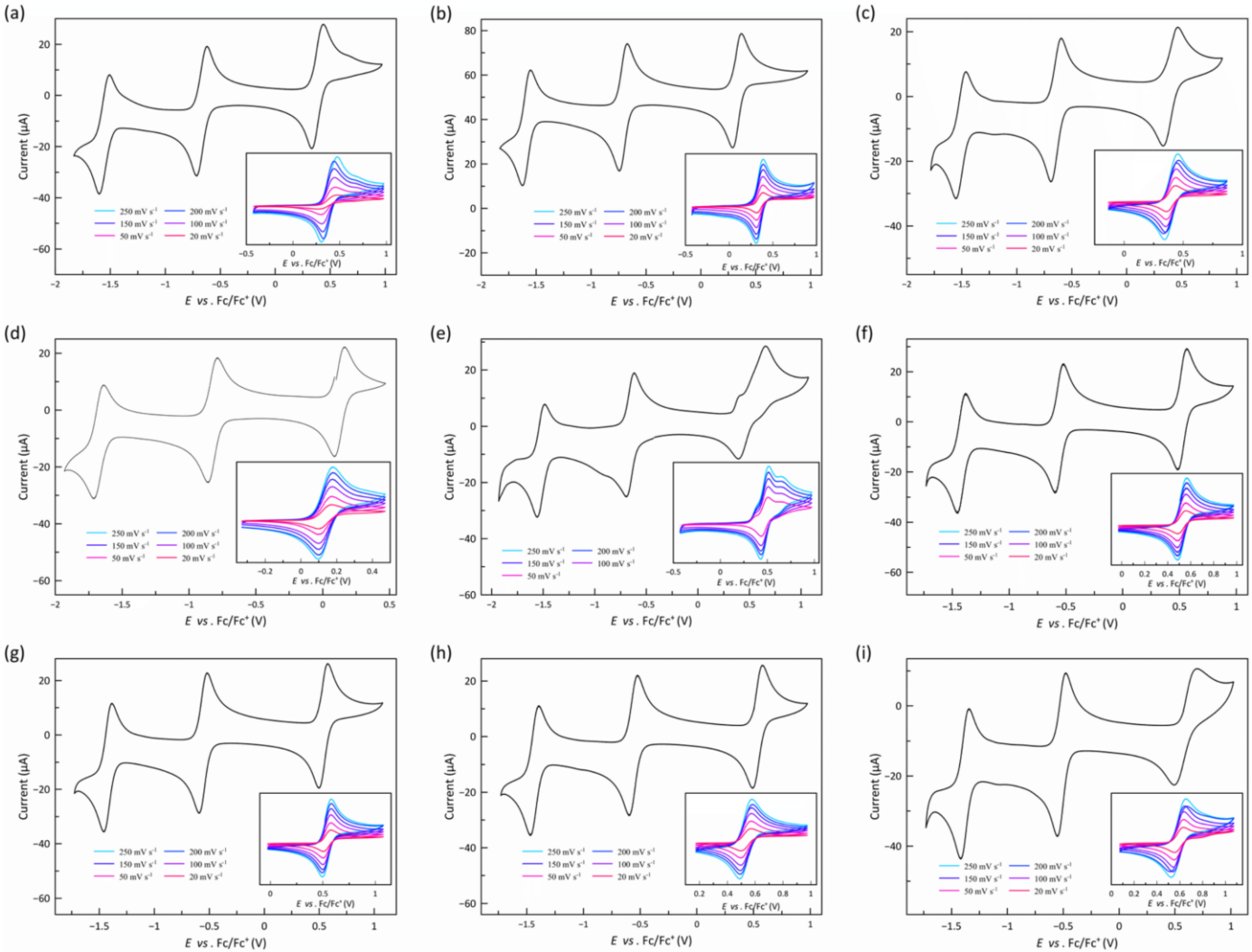

Fig. S25 Cyclic voltammograms of **1**–**9** (a–i) in acetonitrile (0.1 M nBu$_4$NPF$_6$) at 25 ˚C and 200 mV s^{-1}. The insets show the cyclic voltammograms of the oxidation wave in the scan rate range of 20–250 mV s^{-1}.

Table S7. Selected electrochemical data for **1**–**9**[a]

	E_1[b] (V)	E_2[b] (V)	E_3[b] (V)	E_4[b] (V)	E_5[b] (V)	$K_{c,23}$[c] ($\times 10^{-14}$)	$K_{c,45}$[c] ($\times 10^{-3}$)
1	0.38 (105)	–0.67 (93)	–1.55 (93)	–2.06 (i)	-	8.2	-
2	0.33 (83)	–0.71 (71)	–1.59 (73)	–2.02 (i)	–2.19 (i)	8.2	0.8
3	0.40 (137)	–0.64 (95)	–1.51 (93)	–1.95 (i)	-	5.6	-
4	0.14 (88)	–0.82 (77)	–1.67 (83)	–2.10 (i)	-	2.6	-
5	0.52 (260)	–0.65 (76)	–1.52 (71)	–2.04 (i)	-	5.6	-
6	0.53 (78)	–0.56 (73)	–1.42 (76)	–1.88 (i)	-	3.8	-
7	0.54 (80)	–0.56 (71)	–1.42 (78)	–1.88 (i)	-	3.8	-
8	0.54 (85)	–0.56 (78)	–1.42 (78)	–1.88 (i)	-	3.8	-
9	0.59 (202)	–0.52 (76)	–1.38 (73)	–1.85 (i)	-	3.8	-

[a] In acetonitrile (25 °C, 0.1 M nBu$_4$NPF$_6$) with a scan rate of 200 mV s^{-1}. [b] All formal potential (E/V) were taken as the half-wave potentials *vs* Fc$^+$/Fc, except for the irreversible (i) reduction waves for which the cathodic peak potentials are given instead. The peak-to-peak separation (ΔE in mV) between the anodic and cathodic peak potentials are given in parentheses. [c] The comproportionation constant (K_c) were calculated from the E values between the two pairs of one-electron reduction waves ($\Delta E_{23} = E_2 - E_3$ and $\Delta E_{45} = E_4 - E_5$) through the expression $\log K_c = \Delta E/0.059$.

Table S8. Calculated atomic spin densities (ρ) for the cobalt and nitrogen donor atoms of the [$Co^{II}(PDI^{\bullet-})_2$] species in the F and AF states with LS and HS Co^{II} ions

Metal ion	State[a]	ρ_{Co} (e^-)	ρ_{N1} (e^-) [b]	ρ_{N2} (e^-) [b]
LS Co^{II}	F	+1.037	+0.201	+0.234
	AF	–0.947	+0.208	+0.192
HS Co^{II}	F	+2.715	+0.215	+0.210
	AF	+2.620	–0.123	–0.120

[a] F: Ferromagnetic coupling, AF: Antiferromagnetic coupling. [b] Average between the values for the three nitrogen donor atoms from each $PDI^{\bullet-}$ radical (i = 1 and 2)